# Multiple Dolomitization and Fluid Flow Events in the Precambrian Dengying Formation of Sichuan Basin, Southwestern China

PENG Bo[1, 2], LI Zongxing[1, *], LI Guorong[3], LIU Chenglin[4], ZHU Shifa[4], ZHANG Wang[3], ZUO Yinhui[3], GUO Yingchun[1] and WEI Xiaojie[1]

1 *Institute of Geomechanics, Chinese Academy of Geological Sciences, Beijing 100081, China*
2 *Shandong Provincial Key Laboratory of Depositional Mineralization & Sedimentary Mineral, Shandong University of Science and Technology, Qingtao 266590, Shandong, China*
3 *State Key Laboratory of Oil and Gas Reservoir Geology and Exploitation, Chengdu University of Technology, Chengdu 610059, Sichuan, China*
4 *College of Geosciences, China University of Petroleum (Beijing), Beijing 102249, China*

**Abstract:** The Precambrian Dengying Formation is a set of large-scale, extensively dolomitized, carbonate reservoirs occurring within the Sichuan Basin. Petrographic and geochemical studies reveal dolomitization was a direct result of precipitation by chemically distinct fluids occurring at different times and at different intensities. Based on this evidence, dolomitization and multiple fluid flow events are analyzed, and three types of fluid evolution models are proposed. Results of analysis show that Precambrian Dengying Formation carbonates were deposited in a restricted peritidal environment (630–542 Ma). A high temperature and high $Mg^{2+}$ concentration seawater was a direct result of dolomitization for the micrite matrix, and for fibrous aragonite in primary pores. Geochemical evidence shows low $\delta^{18}O$ values of micritic dolomite varying from −1.29‰ to −4.52‰ PDB, abundant light rare earth elements (REEs), and low dolomite order degrees. Microbes and meteoric water significantly altered dolomite original chemical signatures, resulting in algal micritic dolomite and the fine-grained, granular, dolosparite dolomite having very negative $\delta^{18}O$ values. Finely crystalline cement dolomite (536.3–280 Ma) and coarsely crystalline cement dolomite have a higher crystallization degree and higher order degree. The diagenetic sequence and fluid inclusion evidence imply a linear correlation between their burial depth and homogenization temperatures, which closely resemble the temperature of generated hydrocarbon. Compared with finely crystalline dolomite, precipitation of coarsely crystalline dolomite was more affected by restricted basinal fluids. In addition, there is a trend toward a more negative $\delta^{18}O$ value, higher salinity, higher Fe and Mn concentrations, REE-rich. Two periods of hydrothermal fluids are identified, as the exceptionally high temperatures as opposed to the temperatures of burial history, in addition to the presence of high salinity fluid inclusions. The early hydrothermal fluid flow event was characterized by hot magnesium- and silicon-rich fluids, as demonstrated by the recrystallized matrix dolomite that is intimately associated with flint, opal, and microcrystalline quartz in intergranular or intercrystalline pores. This event was likely the result of a seafloor hydrothermal chimney eruption during Episode I of the Tongwan Movement (536.3±5.5 Ma). In contrast, later hydrothermal fluids, which caused precipitation of saddle dolomite, were characterized by high salinity (15–16.05wt% NaCl equivalent) and homogenization temperatures (250 to 265°C), $\delta^{18}O$ values that were more enriched, and REE signatures. Geochemical data and the paragenetic sequence indicate that this hydrothermal fluid was related to extensive Permian large igneous province activity (360–280 Ma). This study demonstrates the presence of complicated dolomitization processes occurring during various paleoclimates, tectonic cycles, and basinal fluids flow; results are a useful reference for these dolomitized Precambrian carbonates reservoirs.

**Key words:** Precambrian, dolomite, geological fluid flow, meteoric water, hydrothermal activity, Sichuan Basin

* Corresponding author. E-mail: lizongxing@cags.ac.cn

# 1 Introduction

Dolomitization in geologic records has been widely discussed because of its significance within carbonate reservoirs in many global oil fields (Jacquemyn et al., 2014; Ronchi, 2012; Zhu Dongya et al., 2015; Li Qing et al., 2016; Husmann, 2016; Bozkaya et al., 2016;Liu Xiaoping et al.,2017;Su Jin et al.,2017). The major parameters controlling dolomitization are fluid chemistry, kinetic factors, formation timing, and multiple fluid flow events. Current literature presents the involvement of most geological fluids in the precipitation of dolomite, including seawater (Wood et al., 2002; Huang Sijing et al., 2011), meteoric water (Li Guorong et al., 2014), formation water (Morrow et al., 1995; Jones et al., 2002), brine fluids (Machel et al., 2002; Davies et al., 2006; Wang Xiaolin et al., 2017; Yuan Jianying et al., 2017; Zhu Shifa et al., 2017), and organic acids (Meng Yuanlin et al., 2014). Furthermore, multiple approaches and models have been proposed to interpret dolomitizing formation under various fluid flow. Although it has also been suggested that dolomitization occurs during exposure to a variety of diagenetic environments, each with different physical and chemical characteristics (Huang Sijing et al., 2009; Liu Shugen et al., 2013), the formation of dolomite remains the subject of much controversy.

Huge reserves of gas are produced from variably dolomitized carbonates in the Precambrian Dengying Formation of the Sichuan Basin (Yuan Haifeng et al., 2014; Xu Guosheng 2013, Liu An et al., 2017). Many researchers have studied the dolomitization of Precambrian carbonate platforms in western China, and various dolomite types have been identified (Wang Guozhi et al., 2009; Shi Zejin et al., 2013). The most widely used model to explain dolomite formation in the Dengying Formation involves evaporation pump dolomitization during depositional stages (Wang Lichao et al., 2014). Based on an analysis of associated minerals (Wang Guozhi et al., 2014), dolomite has been found to occur as cement in filling pores, fractures, and voids, and is interpreted as being closely related to hydrothermal fluids associated with tectonic events in the basin (Jiang Yuqiang et al., 2016; Xi Binbin et al.,2017). However, limited attention has been paid to the relationship between dolomite formation and the fluid evolution of different dolomite phases. In addition, current models of dolomitized fluids are not able to provide an explanation for the entire formation of dolomite within the Dengying Formation. Furthermore, the timing of different dolomitizing diagenetic events remains unclear.

The principal objective of this study, therefore, is to determine the occurrence, distribution, and timing of different dolomite phases and other important diagenetic events occurring in this Formation. The paragenetic sequence between dolomite and associated minerals is discussed, and the sources and chemistry of diagenetic fluids precipitating dolomites are evaluated. The time-constraint on fluid flow is made using the paragenetic sequence, chronological data (Wang Guozhi et al., 2013; Xu Guosheng et al., 2013; Chen Daizhao et al., 2015) and burial and/or tectonic history. Based on an understanding of the relationship between the relative timing of dolomite precipitation and the source of the dolomitizing fluids, models that account for the observed distribution of dolomite types within the Dengying Formation are then proposed.

# 2 Geological Settings

The study area is located in the southern and peripheral parts of the Sichuan Basin (Fig. 1), which is a large-scale, polycyclic, superimposed basin located situated on the South China Yangtze Plate. The target area is the Dengying Formation, Upper Precambrian ($Z_3dy$), which consists of micritic dolomite and algal dolomite and can be divided into four members. The first member ($Z_3dy^1$) comprises mainly micritic dolomite; $Z_3dy^2$ and $Z_3dy^3$ comprise algal dolomites, although algal stromatolite is more developed in $Z_3dy^3$; and $Z_3dy^4$ comprises a set of micritic dolomite featuring highly developed siliceous interlayers and chert bandings (Fig. 2).

The Denying Formation dolomite is overlain by Cambrian Jiulaodong Formation siltstone in most of the Southern Sichuan Basin and is underlain by Doushantuo Formation greywacke, showing an unconformable contact with Cambrian Niutitang Formation shales in the southeastern Sichuan Basin. Multiple tectonic movements have successively affected the study area, including the Chengjiang, Xingkai (Tongwan), Yungui, Yeli, Caledonian, and Hercynian (E'mei) movements (Gu Zhidong et al., 2016); of these, the Xingkai and E'mei Movements contributed to extensional faulting activities, and the Yungui, Yeli, and Caledonian Movements resulted in compressional folding activities. These Paleozoic tectonic activities had a large impact on the sedimentary structure, diagenesis, and reservoir evolution (Li Qigui et al., 2013; Chen Zongqing et al., 2013). In addition, during development of the Dengying Formation, an epicontinental sea carbonate platform was widely distributed within the study area (Zheng Min et al., 2015).

# 3 Samples and Methods

In this study, samples were obtained from outcrops,
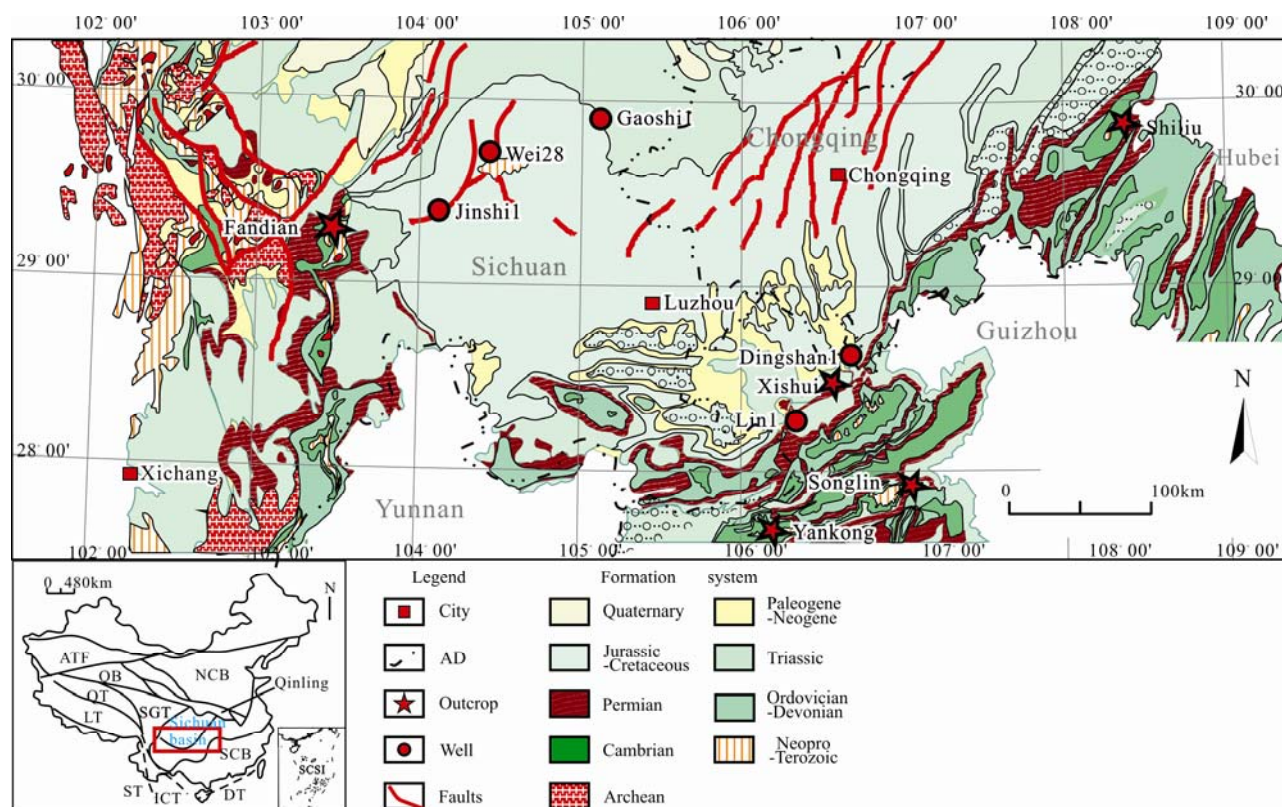
Fig. 1. Geological map of southern Sichuan Basin.
Note: Red dots represent sampling locations of Precambrian Dengying Formation dolomite.

cores, and cuttings in both the eastern and western parts of the southern Sichuan Basin and were selected for comprehensive analyses (see Table 1). We firstly observed the dolomites using a highly magnified glass to distinguish them by color, grain size, texture, and sedimentary structure with reference to Sibley and Gregg's (1987) Dolomite Textural Classification. Pure dolomite thin sections were then selected using alizarin red staining, and a total of 159 thin sections were obtained (Table 1). Through microscopic analysis of crystal shape and optical characteristics, the numbers of all dolomite thin section were confirmed to be larger than or equal to 3.

Several analytical methods were used to determine the compositions of dolomite. Cathodoluminescence analysis was conducted using a rated voltage of 220 Kv and an exposure duration of 10 s for image acquisition at Chengdu University of Technology, to further identify cements with different diagenetic sequences by analyzing the ratio of $Fe^{2+}$ over $Mn^{2+}$.

Electron microprobe analysis was conducted using a Shimadzu EPMA-1600 instrument with an accelerating voltage of 15 kv and a specimen current of 20 nA at the Southwest Mineral Resources Supervision and Monitoring Center, China's Ministry of Land and Resources. The detection limits of the microprobe were estimated at approximately 0.002 element %. Results were then combined with those of cathodoluminescene analysis by comparing $Fe^{2+}/Mn^{2+}$ ratios obtained using these two types of analyses, to distinguish dolomites and determine compositional differences.

Rare earth element (REE) and dolomite order-degree analyses were conducted to investigate differences in the geochemical characteristics between the different dolomite types. Samples were taken using a Miniature Bur from the fresh surface of rocks at places where thin sections were obtained, using a sample weight of 1 g for REE analysis and 5 g for dolomite order-degree analysis. Analysis of trace REE was conducted using an ICP-MS instrument at the Australian Laboratory Services, at a temperature of 22ºC and humidity of 58% and with an analytical error limited to less than 10%; dolomite order-degree analysis was conducted at Chengdu University of Technology at a temperature of 20ºC and humidity of 58%.

Analyses of carbon and oxygen stable isotopes and fluid inclusions were implemented to distinguish the different types of dolomites, and these analyses also revealed diagenetic fluid properties by calculating the $\delta^{18}O$ value of these calcareous cement based on the principle of isotope fractionation. Carbon and oxygen stable isotopic analyses were accomplished using a MAT-252 mass spectrometer at the geological laboratory of the Exploration and Development Research Institute, PetroChina Southwest
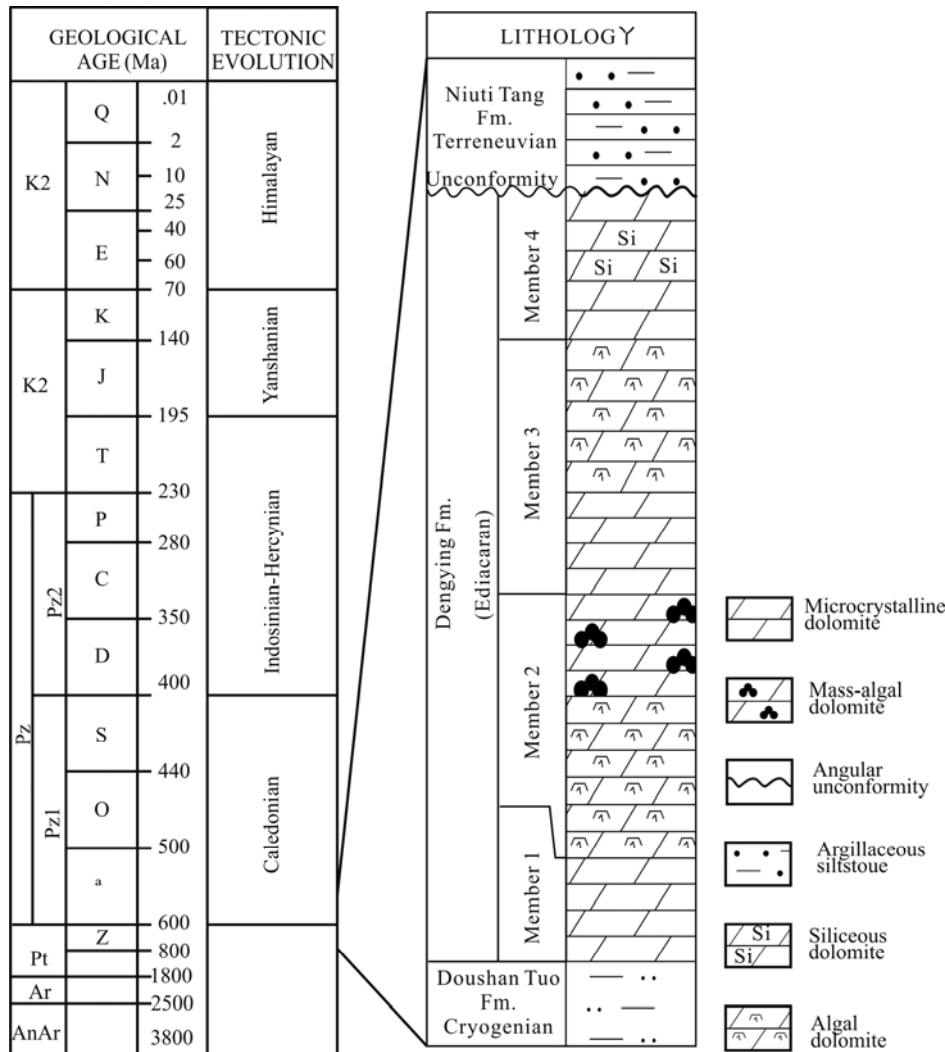
Fig. 2. Generalized stratigraphic column of Dengying formation in Sichuan Basin.

**Table 1 Geochemical information of Precambrian Dengying Formation dolomite samples from southern Sichuan Basin**

| Sections | Sampling points | Matrix | Fillings | Wells | Sampling points | Matrix | Fillings |
|---|---|---|---|---|---|---|---|
| Fandian | Fandian, Leshan | 8 | 36 | Well Jinshi1 | Qianwei, Leshan | 3 | 11 |
| Yankong | Jinsha, Guizhou | 11 | 48 | Well Dingshan1 | Qijiang, Chongqing | 0 | 5 |
| Songlin | Zunyi, Guizhou | 1 | 5 | Well Lin1 | Xishui, Guizhou | 1 | 10 |
| Xishui | Xishui, Guizhou | 3 | 8 | Well Gaoshi1 | Anyue, Ziyang | 2 | 11 |
| Shiliu | Shizhu, Chongqing | 5 | 25 | | | | |

Oil & Gasfield Company, using 33 micro-samples (10–50 mg) taken from cut dolomite surfaces with a dental drill (Table 2). The powdered micro-samples were reacted with 100% orthophosphoric acid at 50ºC for 3 h under vacuum to produce $CO_2$ gas, and the carbon and oxygen ratios of the equilibrated $CO_2$ gas were determined using a VG 903 Micromass gas source stable isotope ratio mass spectrometer with an analytical precision better than 0.011. Isotope data were reported in standard notation relative to standard PDB for carbon ratios and SMOW for oxygen ratios, and $\delta^{18}O$ (SMOW) values were then converted $\delta^{18}O$ (PDB) values. Fluid inclusions were analyzed using a British Linkam MDS 600 cooling-hearting stage (equipped with Carl-Zeiss Axioplan 2 microscope) at Chengdu University of Technology. A total of 47 fluid inclusion thin sections were prepared based on thin section observation results, which encompassed the main dolomite types. The temperature test error varied with experimental temperatures, which were ± 0.1 ºC, ± 0.5 ºC, and ± 1 ºC, respectively, and corresponded to temperature ranges of less than 0 ºC, from 0 to 30 ºC, and larger than 30 ºC, respectively. The rate of temperature rise was firstly controlled within 10 ºC/min during the test stage, and then within 1 ºC/min when the temperature reached the critical phase transition temperature, using temperature precision and stability of 0.01ºC/<0.01ºC. However, due to multi-stage diagenesis and mineral composition of the dolomites analyzed, original fluid

**Table 2 Classification and geochemical characteristics of dolomites in the matrix**

| Sample No. | Strata | Test object | $\delta^{13}$C (‰PDB) | $\delta^{18}$O (‰PDB) | Order degree | Sample No. | Strata | Test object | $\delta^{13}$C (‰PDB) | $\delta^{18}$O (‰PDB) | Order degree |
|---|---|---|---|---|---|---|---|---|---|---|---|
| FD-Zd-12 | $Z_3dy^1$ | MD1 | 3.27 | −1.29 | 0.68 | YK-Z-168 | $Z_3dy^3$ | MD2 | 1.6 | −4.36 | 0.5 |
| FD-Zd-14 | $Z_3dy^1$ | MD1 | 1.83 | −4.38 | | YK-Z-86 | $Z_3dy^2$ | MD2 | 3.84 | −4.6 | 0.92 |
| FD-Zd-15 | $Z_3dy^1$ | MD1 | 3.55 | −1.89 | | JS1-6-75\75 | $Z_3dy^3$ | MD2 | 4.16 | −5.16 | |
| FD-Zd-41 | $Z_3dy^2$ | MD1 | 2.68 | −3.59 | 0.54 | YK-Z-93 | $Z_3dy^2$ | MD2 | 4.41 | −6.81 | 0.71 |
| YK-Z-14 | $Z_3dy^2$ | MD1 | 7.14 | −4.52 | 0.61 | FD-Zd-30 | $Z_3dy^1$ | MD2 | 1.5 | −7.49 | |
| YK-Z-20 | $Z_3dy^2$ | MD | 6.64 | −3.48 | | FD-Zd-36 | $Z_3dy^1$ | MD2 | 1.75 | −5.74 | 0.69 |
| YK-Z-36 | $Z_3dy^2$ | MD1 | 6.6 | −3.58 | | JS1-6-34\75 | $Z_3dy^3$ | MD2 | 3.9 | −5.47 | 0.63 |
| YK-Z-56 | $Z_3dy^2$ | MD1 | 5.03 | −2.41 | 0.54 | YK-Z-184 | $Z_3dy^3$ | MD3 | 1.4 | −4.94 | 0.43 |
| YK-Z-60 | $Z_3dy^2$ | MD1 | 4.46 | −2.13 | 0.57 | JS1-5-1\35 | $Z_3dy^3$ | MD3 | 1.8 | −6.77 | 0.66 |
| YK-Z-112 | $Z_3dy^2$ | MD1 | 3.29 | −1.95 | 0.57 | FD-Zd-23 | $Z_3dy^1$ | MD3 | 3.23 | −6.52 | |
| YK-Z-122 | $Z_3dy^2$ | MD1 | 4.84 | −2.28 | | FD-Zd-54 | $Z_3dy^3$ | MD3 | −0.76 | −6.97 | 0.83 |
| YK-Z-137 | $Z_3dy^3$ | MD2 | 1.86 | −3.93 | 0.52 | FD-Zd-51 | $Z_3dy^2$ | MD3 | −1.3 | −8.51 | |
| FD-Zd-13 | $Z_3dy^1$ | MD2 | 2.76 | −3.09 | | TZd45-2 | | MD3 | 2.66 | −8.38 | 0.96 |
| JS1-6-6\75 | $Z_3dy^3$ | MD2 | 4.23 | −3.7 | | SLZd1-15 | | MD3 | 5.29 | −6.47 | |
| YK-Z-114 | $Z_3dy^2$ | MD2 | 2.97 | −3.16 | 0.71 | SLZd1-17 | | MD3 | 4.91 | −6.14 | |
| YK-Z-129 | $Z_3dy^3$ | MD2 | 1.56 | −3.68 | | SLZd1-32 | | MD3 | 3.51 | −5.3 | |
| YK-Z-19 | $Z_3dy^2$ | MD2 | 6.79 | −3.59 | | | | | | | |

Note: MD1, Micritic matrix dolomite, MD2, Algal micritic matrix dolomite, MD3, Finely crystalline matrix dolomite.

inclusions were not found in all early-filled dolomites.

## 4 Results

### 4.1 Petrography and paragenetic sequence

Based on an examination of crystal size, distribution, and crystal surface shape (planar or nonplanar) (Friedman & Sanders, 1967；Jones et al.,2002;Lippmann et al., 2012;Beckert et al.,2015;Alonso-Zarza et al.,2016), three types of matrix dolomite textures were recognized from the Precambrian Dengying Formation in the Sichuan Basin: (1) micritic dolomite (Md1), (2) algal micritic dolomite (Md2), and (3) finely crystalline matrix dolomite (Md3). In addition, six types of cement dolomites were recognized: (1) fibrous dolomites, (2) fine-grained, granular dolosparite, (3) bladed dolomite, (4) finely crystalline dolomite, (5) coarsely crystalline dolomite, and (6) saddle dolomite.

### 4.1.1 Matrix dolomite

Micritic dolomite crystals are generally present at sizes of less than 25 μm (Fig. 3a) with planar-a and planar-s fabrics. They occur in mud-supported fades, which were originally precipitated without a biological structure, and can be distinguished from algal micritic dolomite. Under cathodoluminescence, micritic dolomite is nonluminescent to very dull-red luminescent (Fig. 3b). Micritic dolomite is the major crystal type of matrix dolomite and usually accounts for more than 60% of the total rock volume in the Dengying Formation.

Finely crystalline matrix dolomites range in size from 25–250 μm (Fig. 3c) and exhibit planar-a and planar-s sucrosic textures (Jeff Lonnee and Ihsan S. Al-Aasm, 2000). Cathodoluminescence colors are generally bright red (Fig. 3d). Volumetrically, this type of dolomite accounts for about 20% by volume of all matrix dolomites.

Algal micritic dolomite occurs generally at a size of 2–40 μm (Fig. 3e) and is characteristically associated with fibrous dolomite (FD) and mimic algal structures in the Dengying Formation (Lei Huaiyan et al., 1992；You Xuelian et al., 2013). Under cathodoluminescence, algal micritic dolomite has a brighter light than micritic dolomite (Fig. 3f), which indicates a more intimate relationship between its precipitation and biological activity (You Xuelian et al., 2015).

Variations in their occurrences are attributed to the associated sedimentary facies and internal biological activities.

### 4.1.2 Cement dolomite

Multiple cement dolomites are identified by crystal size, crystal shape, and paragenesis, and they partially or completely fill dissolution vugs and fractures (Fig. 4).

Fibrous dolomites are usually precipitated at the margin of dissolution vugs and fractures, or along dolomite breccias, but are most common at the margin of primary pores and vugs and on the surfaces of large grape-like dolomite fractures and vugs (Lian Chengbo et al., 2016). Granules, micrite, and breccia have an equiaxial zonal structure, with a length-width ratio reaching more than 10 μm and an axial length of 80–600 μm, and show wavy extinction characteristics under orthogonal light and a dark red light under cathodoluminescence (Fig. 3f).

The fine-grained, granular, dolosparite has a hypautomorphic structure, is often precipitated in an algal window-like pore-cavity, algal lamina, and syngenetic breccias (Lin Xiaoxian et al., 2017), and is generally wrapped by FDs. It was generated during the penecontemporaneous stage rather than in the late stage of
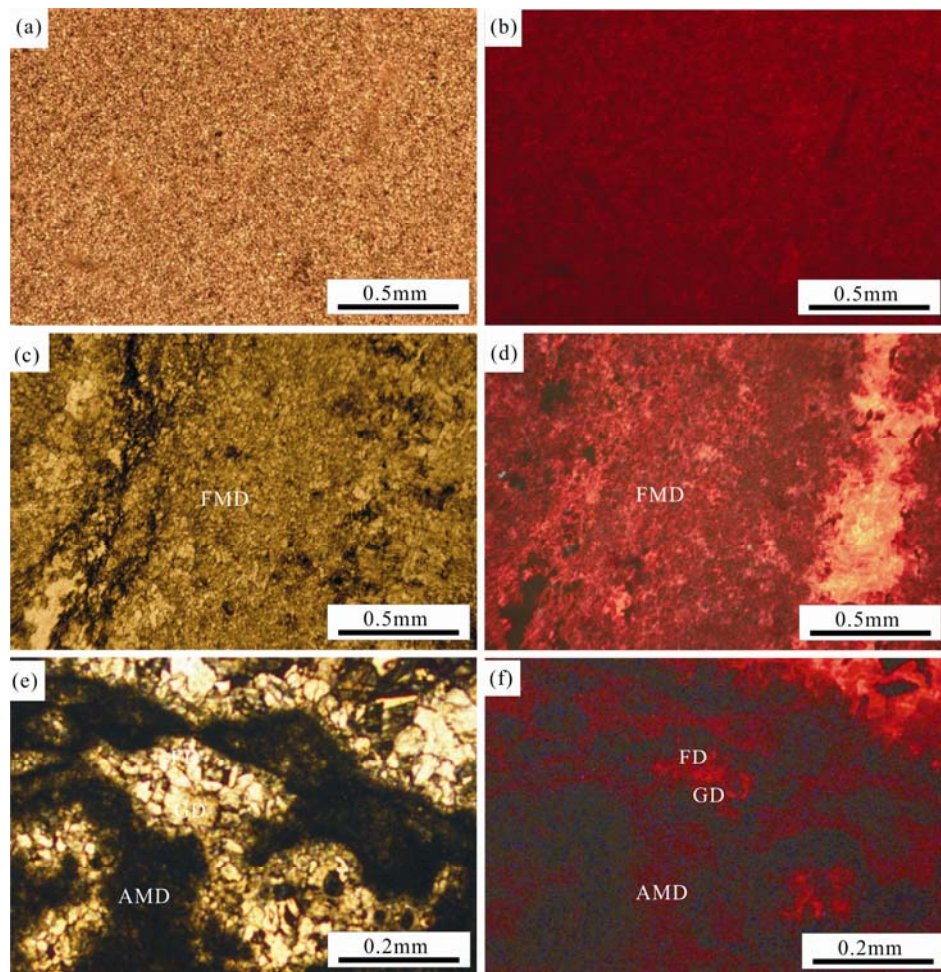
Fig. 3. Microscopic images of different matrix dolomites.
(a), Photomicrograph of micritic dolomite, Fandian Section, Z3dy, FD-92, plane-polarized light; (b), Cathodolumi-
nescence (CL) photomicrograph of (a); (c), Photomicrograph of finely crystalline matrix dolomite (MD3), Shiliu
Section $Z_3dy$, TZD18-1, plane-polarized light; (d), Cathodoluminescence (CL) photomicrograph of (e); Photomi-
crograph of algal micritic dolomite, with fibrous dolomite (FD) and granular sparry dolomite fillings in window-
like pores, plane-polarized light; (f) Cathodoluminescence (CL) photomicrograph of (e).

fracture-cavity, and displays nonluminescence to very dull
-red luminescence under cathodoluminescence (Fig. 3f).

Bladed dolomite was generally precipitated in either
large dissolution seams or in certain large window-like
primary pores. It mostly occurs along the margins of
fractures and vugs alone, or is associated with FD, where
it grows along FD rims with a length-width ratio of 10 μm
(Fig. 4a). The crystal size is variable in different locations:
approximately 200 μm in window-like pores and vugs, but
over 2000 μm in some dissolution seams. It displays
nonluminescence under cathodoluminescence but emits
weak light under an electron probe (Fig. 4b).

Finely crystalline dolomite was precipitated in
dissolution fractures and vugs, or along surfaces of
fractures and vugs. It commonly fills bladed dolomite, or
directly fills fractures and vugs (Fig. 4c). Granular
dolomite exists in a detachment layer and emits a red color
at the margin but no light in intra-particles under

cathodoluminescence (Fig. 4d). The finely crystalline
dolomite in dissolution fractures and vugs displays
nonluminescence to very dull-red luminescence under
cathodoluminescence.

Coarsely crystalline dolomite was precipitated in
dissolution vugs and has a mosaic symbiotic relationship
with euhedral dolomite. It may have been formed by
dynamic crystallization in the late stage; this is
demonstrated by the complementary lamellar structure and
flat contact margin. The euhedral mineral has a rhombic
geometry and consists of a few argillaceous and impure
components. The particles are clean, with an interference
color of high-order white that is colorless under polarized
light (Fig. 4c). Two groups of rhombus intersection
cleavages are clearly observed, representing symmetry
extinction along the cleavage direction. Associated
minerals and accessory minerals are rarely observed.

Saddle dolomite was the last dolomite phase to
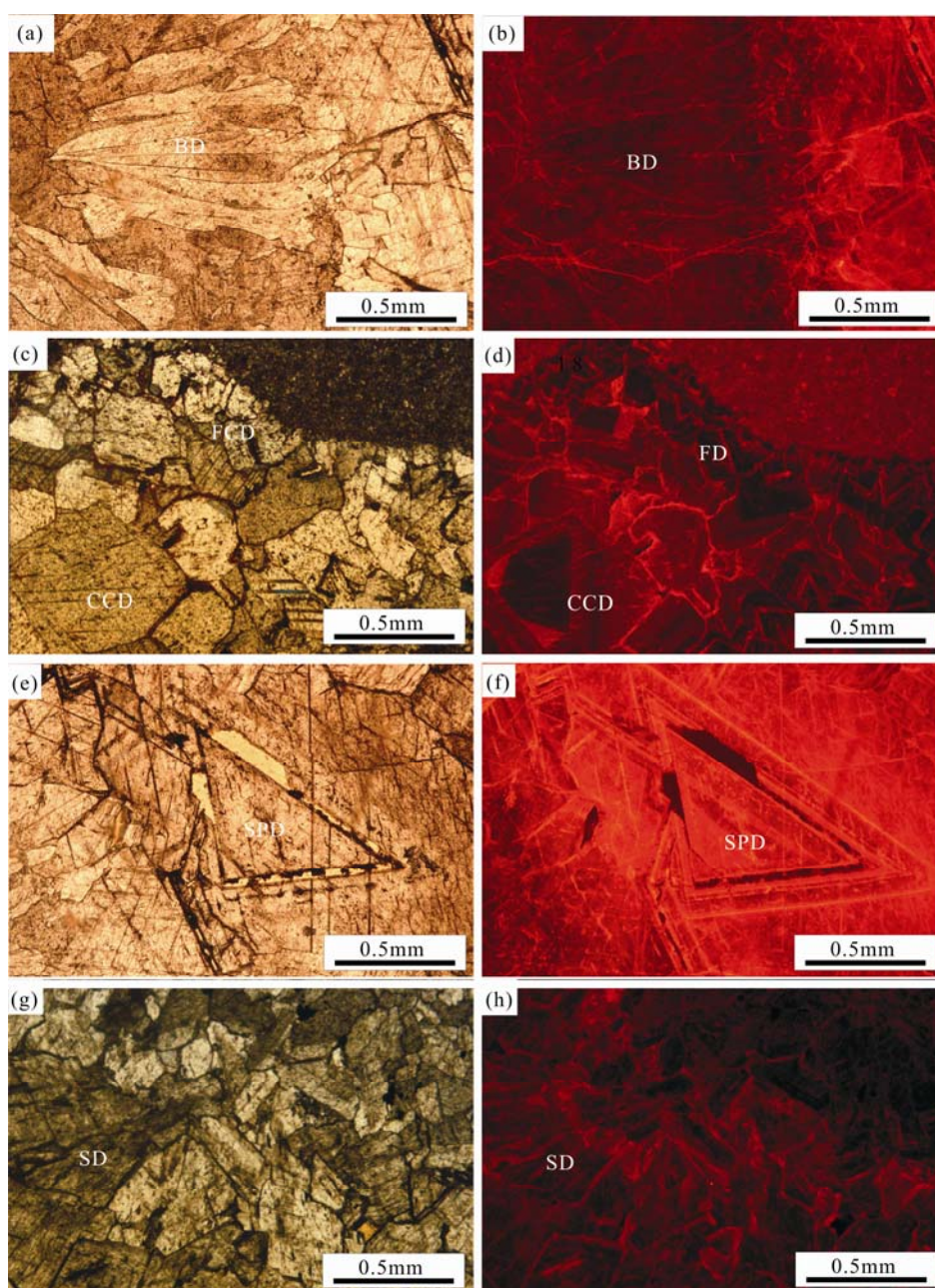
Fig. 4. Microscopic images of cement dolomite.
(a), Photomicrograph of bladed dolomite (BD) with radial growth, plane-polarized light; (b), Cathodoluminescence (CL) photomicrograph of (a); (c), Photomicrograph of finely crystalline dolomite (FCD) and coarsely crystalline dolomite (CCD) filling in fractures and vugs, plane-polarized light; (d), Cathodoluminescence (CL) photomicrograph of (C); (e), Photomicrograph of schistic dolomite (SD) overgrowth, plane-polarized light; (f), Cathodoluminescence (CL) photomicrograph of schistic dolomite displaying red with lighter orange luminescence, Dengying Formation, rock borehole 213–02; (g), Coarsely crystalline saddle dolomite (SD) in fracture-cavity, Precambrian Dengying Formation, rock borehole 344-YK, 10×5 (−); (h), Saddle dolomite emitting dark red light under cathodoluminescence, Precambrian Dengying Formation, rock borehole 344-YK, 10 × 5 (CL).

precipitate and is an indicator of hydrothermal fluids (Jiang Yuqiang et al., 2016). It has a significant symbiotic relationship with quartz, hexagonal columnar calcite, and other heavy minerals, and occasionally consists of organic matter (OM) and hydrothermal fracture breccia. It often occurs in dissolution fractures, vugs, and structural fractures (Haeri-Ardakani,2013), where it cuts country

rock and early dissolution fractures. Dolomite phenocryst presents as massive subhedral crystals under a microscope with coarse grains up to 4000 μm in diameter. It is colorless or turbid-gray under polarized light (Fig. 4g) with an interference color of high-order white. Under microscope, 60–120° rhombus intersection cleavages are observed and show wavy extinction along the cleavage

direction. Crystals are intensively fractured and cracks have developed, which may have been caused by local tectonic stress (Zhang Juntao et al., 2009).

### 4.1.3 Typical associated minerals

(1) Siliceous rocks. These filled pores after granular dolosparite was precipitated, and occurred at approximately the same time as precipitation of bladed dolomite and siliceous dolomite. They mainly occur in bedding-parallel development forms in $Z_3dy^4$ and fill primary pores, early fractures, and vugs. Silica occurs in chert, opal, and micritic dolomites (Fig. 5a), and it partly replaces both matrix dolomite in remnant patch forms and euhedral dolomite (in fractures and vugs) in imitation replacement forms (Fig. 5b).

(2) Asphaltum. This occurred during two phases of the Dengying formation. The first asphaltum phase filled-in pores following the paragenetic sequence of bladed dolomite; this occurred prior to the filling of schistic dolomite but roughly near to the paragenetic sequence of finely crystalline dolomite (FCD). A small amount only is found, and there is no evidence of a previous block mass. This phase of asphaltum filled fractures and vugs, has a circular shape (Fig.5c), and represents an early hydrocarbon migration event. The latter phase of asphaltum filled pores after the precipitation of coarse crystalline dolomite and prior to the filling of saddle dolomite (SD). This OM phase is seen in multiple sections, where it fills the central part of late fractures and vugs in the form of massive asphalt (Fig. 5d).
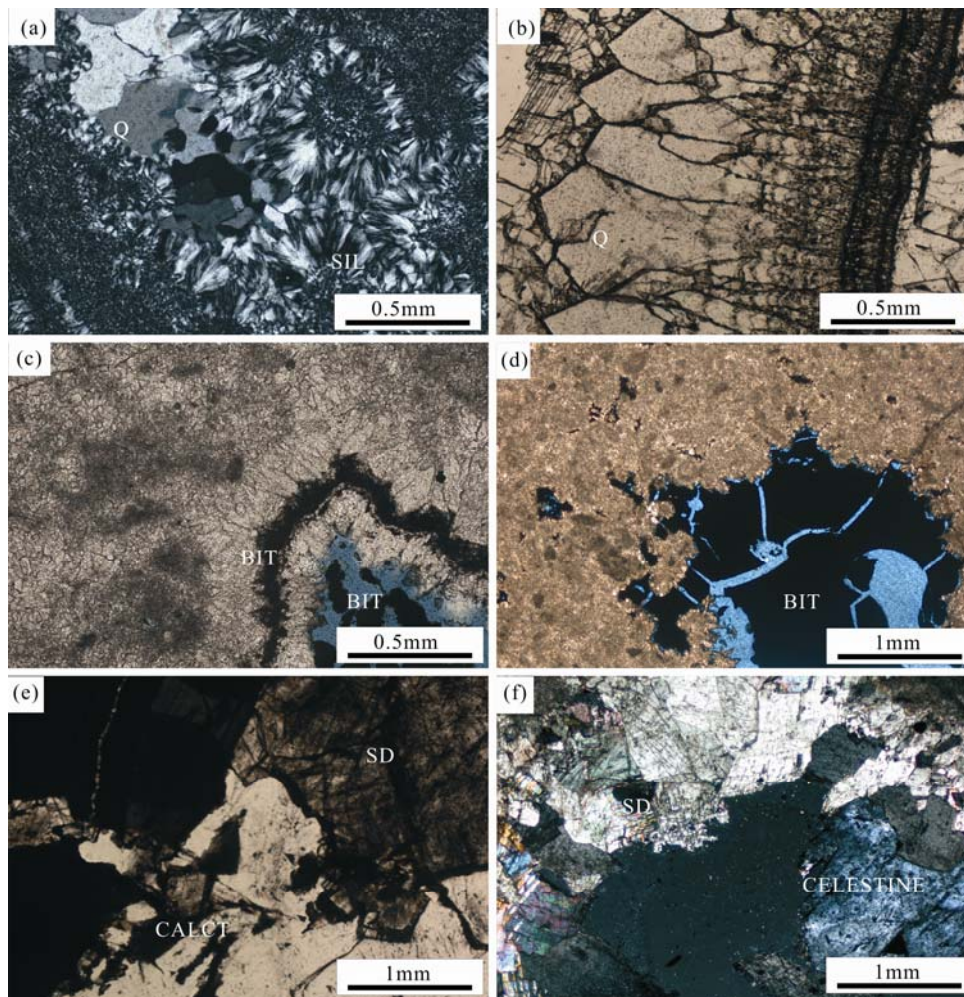


Fig. 5. Associated mineral chart.

(a), Early chert and opal filling fractures and vugs (SIL) associated with siliceous metasomatism, Fandian Section, $Z_3dy^2$, magnification 10X+; (b) Bladed quartz (Q) filling fractures and vugs after filling of fibrous dolomite and prior to filling of middle to coarsely crystalline dolomite, resulting from penecontemporaneous siliceous metasomatism, Fandian section, $Z_3dy^2$, magnification 10X−; (c), Two stages of organic matter filling. The first-stage asphalt (BIT) is circle-shaped, and it filled after the filling of fibrous, granular dolosparite; while the second-stage organic matter filled central fractures and vugs in massive forms, gs1-54, $Z_3dy^2$, magnification 10X−; (d), Late-staged organic matter (asphalt) filling central fractures, vugs, and intergranular holes, gs1-52, $Z_3dy^3$, magnification 10X−; (e), Hexagonal columnar calcite (CALCT) filling fractures and vugs after filling of saddle dolomite (SD), Yankong Section, $Z_3dy^3$, magnification 2.5 X-; (f), Celestite (CELESTINE) filling after filling of saddle dolomite, Yankong Section, $Z_3dy^3$, magnification 2.5X+.

(3) Hexagonal columnar calcites. These have two perfect cleavages, a light-yellow color, hexagonal columnar shape, and produce significant foaming with acid. They are generally thought to have been precipitated by low temperature thermal fluids during the later cement phase. They are commonly observed in large-scale dissolved fractures and vugs in association with saddle dolomites (Fig. 5e) and are followed by the latest stage of euhedral quartz.

(4) Euhedral quartz. Multiple-staged euhedral quartz exists in the paragenesis. However, two stages are dominant: one granular quartz stage filled after bladed dolomite filling, and contributed a small proportion to the total mineral composition. The other euhedral quartz stage is more commonly seen; it filled large fractures and vugs after filling of saddle dolomites, and is found as coarse- to mega-crystals.

(5) Lead-zinc ore. This infilled pores after saddle dolomite filling and was the final filling mineral. It generally occurs in structural fractures and is normally associated with fluorite, pyrite, and euhedral quartz.

(6) Celestite. This is less exposed but occurred in large dissolved fractures and vugs after filling of saddle dolomite and euhedral quartz (Fig. 5f).

### 4.1.4 Paragenetic sequence

Based on diagenetic sequence analyses of 159 thin sections and rock samples from wells and outcrops, the paragenetic sequence can be summarized as follows (Fig. 6): fibrous dolomites; granular sparry dolomite; bladed dolomite; chert and siliceous dolomite; first-staged organic matter; finely crystalline dolomite; schistic dolomite; CCD; second staged organic matter; SD; hexagonal columnar calcite; lead-zinc ore, fluorite, euhedral quartz, and pyrite.

### 4.2 Geochemistry
### 4.2.1 Matrix dolomite

(1) **Micritic dolomite.** Geochemical data show variations in $\delta^{18}O$ values of micritic dolomite between −1.29‰ and −4.52‰ PDB, with an average of −2.95‰ PDB. High salinity in the dolomitization environment led to fast crystallization rates, and the low-order degrees range from 0.52 to 0.68, with an average value of 0.58. It is considered that the low $Fe^{2+}$ content (0.04–0.06 ppm) and $Mn^{2+}$ content (0.01 ppm), which were produced in a low energy environment, promote the dark red color seen under cathodoluminescence (Fig. 3b). REE analysis implies that this type of dolomite contains abundant light REEs and is characterized by a weak-positive Ce anomaly and weak-negative Eu anomaly (Fig. 7a).

(2) **Finely crystalline dolomite.** The $\delta^{18}O$ values are relatively low and range from −4.94‰ to −8.51‰ PDB, averaging −6.74‰ PDB. The order degree is obviously enhanced, ranging from 0.82 to 1.00 and averaging 0.86, which is higher than those of two dolomite types referred to above. The proportions of REEs are higher than that of micritic dolomite, and are close to those of algal micritic dolomite. Negative Ce and Eu anomalies indicate a long-lasting and strong dolomitization process (Fig. 7a).

(3) **Algal micritic dolomite.** This type of dolomite has two different degrees of dolomitization. Geochemical data
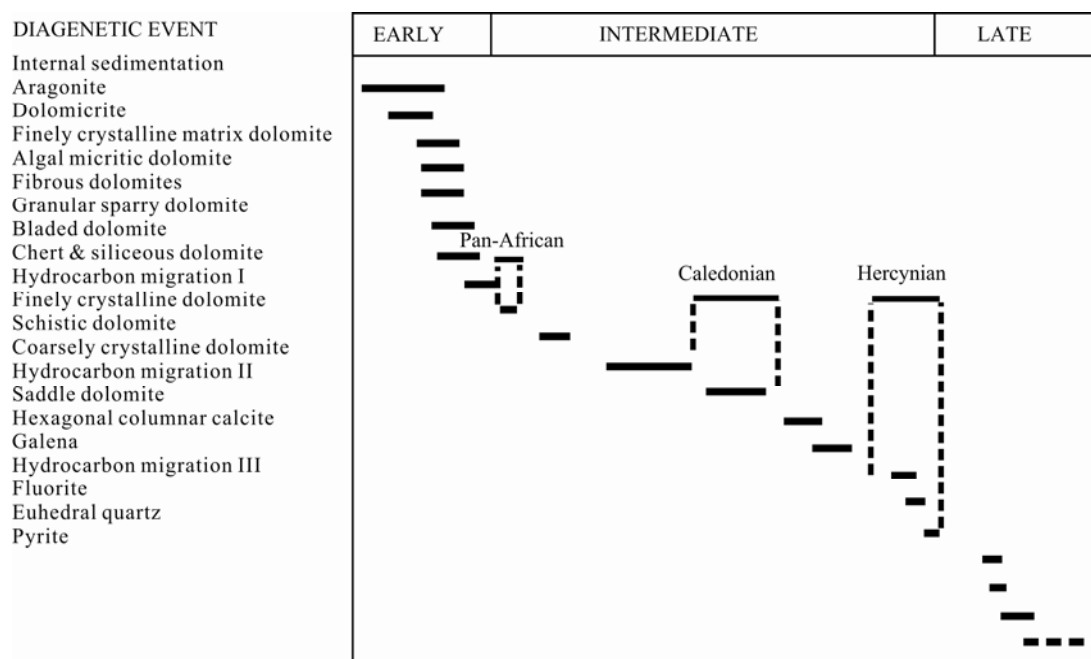


Fig. 6. Paragenetic sequence of Dengying Formation with respect to age and orogenic events.
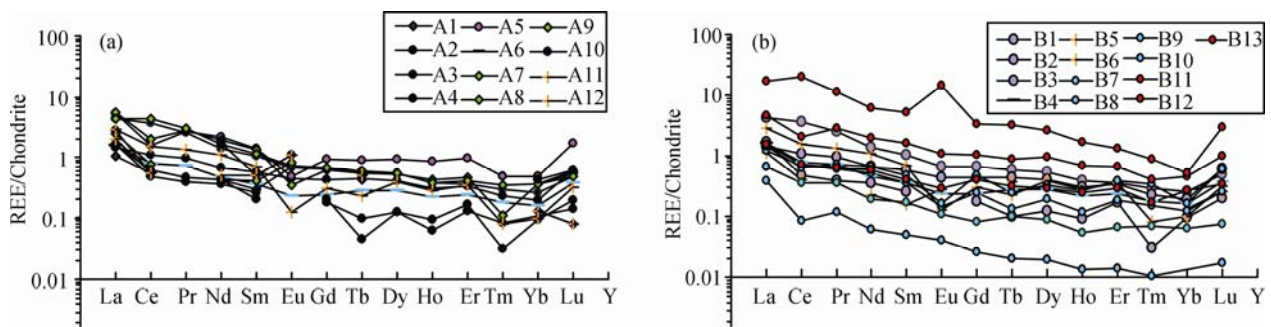
Fig. 7. Distribution of rare earth elements (REEs) in Dengying Formation dolomites within the Sichuan Basin

a, Dolomite in matrix; b, Dolomite in fractures and vugs; a1–a5, Micritic dolomite; a6–a7, Algal micritic dolomite; a8–a9, Finely crystalline dolomite; B1–B3, Micritic dolomite; B4, Granular dolosparite; B5–B6, Acicular columnar dolomite; B7–B8, Finely crystalline dolomite; B9–B10, Middle crystalline dolomite; B11–B13, Saddle dolomite.

reveal that $\delta^{18}O$ values vary from −3.09‰ to −4.60‰ PDB with the lower dolomitization degree (from 0.47 to 0.63) and REE enrichment approaches the micritic dolomite trend line. In contrast, the $\delta^{18}O$ values of this kind of dolomite with a higher dolomitization degree (from 0.69 to 0.92) vary from −5.16‰ to −7.49‰ PDB. The REE enrichment trend line is removed from that of micritic dolomite. In addition, the highly dolomitized algal micritic dolomites are characterized by a negative Eu anomaly, relatively high $Mn^{2+}$ content, and have a dark-red light under cathodoluminescence (Fig. 3f), which can be attributed to a tectonically high position that is vulnerable to strong dolomitization and biological functions (Lei Huaiyan and Zhu Lianfang, 1992; You Xuelian et al., 2014).

### 4.2.2 Cement dolomite

**Fibrous dolomite.** The $\delta^{18}O$ values range from −1.25‰ to −3.78‰ PDB (average −2.56‰ PDB) (Fig. 8), with an order degree ranging from 0.55 to 1.00 (average 0.73) (Table 3). REEs have a low degree of enrichment similar to that of dolomicrite (Fig. 7b).

**Fine-grained, granular dolosparite.** The $\delta^{18}O$ values range from −12.06‰ to −10.98‰ PDB (average −11.42‰ PDB) (Fig. 8), which are significantly different from those of the adjacent fibrous rims, and may be related to blue-green algae activity and meteoric water in the syndiagenetic stage (Shi Zejin et al., 2013). The order degree is between 0.59 and 0.61 (average 0.60) (Table 3).

**Bladed dolomite.** The manganese content is low at less than $20 \times 10^{-6}$. The $\delta^{18}O$ values range from −2.17‰ to 4.23‰ PDB (Fig. 8), the order-degree values range from
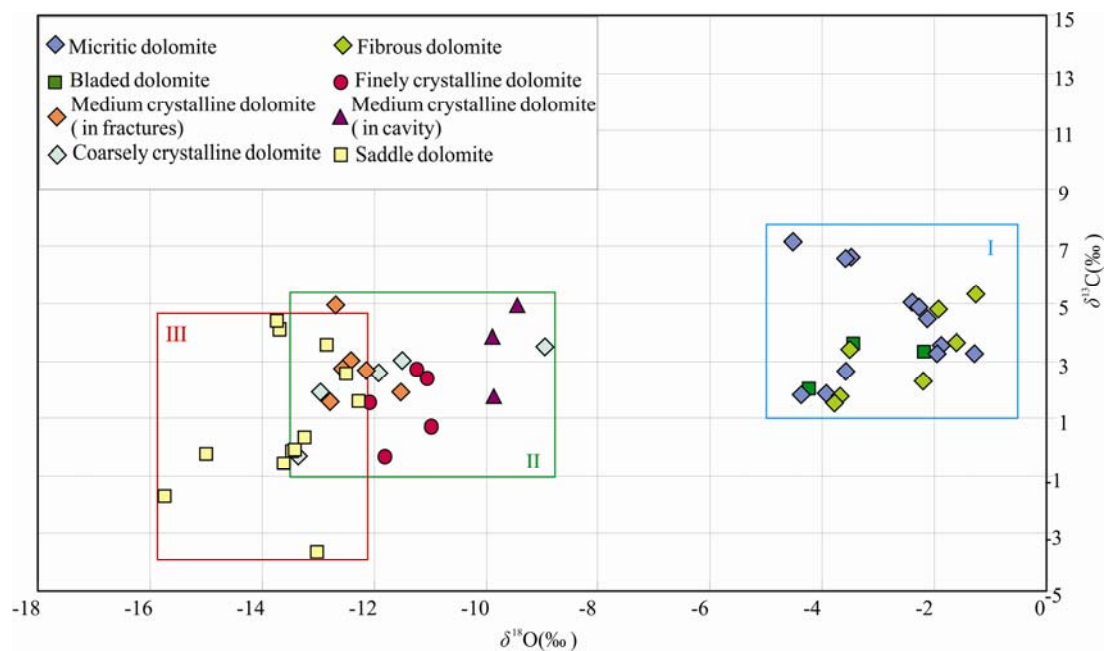


Fig. 8. $\delta^{13}C$ versus $\delta^{18}O$ for dolomite in fractures and vugs.

Zone I, Projection zone of matrix dolomite; dolomites in this zone share similar stable isotope characteristics with matrix dolomite; Zone II, Projection zone of diagenetic fluid action; dolomites in this zone have significantly different stable isotope characteristics to matrix dolomite; Zone III, Projection zone of fluid anomaly; dolomites in this zone have lower $\delta^{18}O$ and higher $\delta^{13}C$ than those in Zone II.

**Table 3 Classification and geochemical characteristics of cement dolomites in Dengying Formation, Sichuan Basin**

| Sample No. | Strata | Lithology | $\delta^{13}C$ (‰PDB) | $\delta^{18}O$ (‰PDB) | Order degree | Sample | Strata | Lithology | $\delta^{13}C$ (‰PDB) | $\delta^{18}O$ (‰PDB) | Order degree |
|---|---|---|---|---|---|---|---|---|---|---|---|
| FD-Zd-3a | $Z_3dy^1$ | FD | 1.77 | −3.69 | | YK-Z-147 | $Z_3dy^3$ | CCD | 1.61 | −12.78 | 0.76 |
| FD-Zd-3b | $Z_3dy^1$ | FD | 2.29 | −2.21 | 0.62 | YK-Z-102 | $Z_3dy^2$ | CCD | 1.76 | −9.86 | |
| FD-Zd-23 | $Z_3dy^1$ | FD | 1.52 | −3.78 | 0.74 | YK-Z-20 | $Z_3dy^2$ | CCD | 3.88 | −9.9 | |
| YK-Z-38 | $Z_3dy^1$ | FD | 5.36 | −1.25 | 0.72 | YK-Z-29 | $Z_3dy^2$ | CCD | 4.96 | −9.45 | 1 |
| YK-Z-39 | $Z_3dy^1$ | FD | 4.81 | −1.92 | | YK-Z-119 | $Z_3dy^2$ | CCD | 3.5 | −8.95 | |
| YK-Z-43 | $Z_3dy^1$ | FD | 3.41 | −3.51 | 0.58 | YK-Z-137 | $Z_3dy^3$ | CCD | 1.9 | −12.96 | 0.84 |
| YK-Z-86 | $Z_3dy^1$ | FD | 3.63 | −1.6 | 0.87 | YK-Z-26 | $Z_3dy^2$ | CCD | 3.04 | −11.5 | 0.75 |
| YK-Z-100 | $Z_3dy^1$ | BD | 2.02 | −4.23 | | YK-Z-36 | $Z_3dy^2$ | CCD | 2.62 | −11.92 | 1 |
| YK-Z-20 | $Z_3dy^1$ | BD | 3.33 | −2.17 | 0.55 | FD-Zd-31 | $Z_3dy^1$ | CCD | −0.32 | −13.32 | |
| YK-Z-74 | $Z_3dy^1$ | BD | 3.59 | −3.44 | 0.43 | FD-Zd-3 | $Z_3dy^1$ | SD | −0.6 | −13.61 | 1 |
| FD-Zd-36 | $Z_3dy^1$ | GSD | 0.73 | −10.98 | 1 | FD-Zd-30 | $Z_3dy^1$ | SD | −0.15 | −13.44 | |
| JS1-5-1\35 | $Z_3dy^1$ | GSD | −0.34 | −11.8 | 0.6 | FD-Zd-32 | $Z_3dy^1$ | SD | 0.32 | −13.24 | |
| JS1-6-75\75 | $Z_3dy^1$ | GSD | 2.7 | −11.23 | 0.63 | FD-Zd-7 | $Z_3dy^1$ | SD | −0.09 | −13.39 | 0.88 |
| YK-Z-18 | $Z_3dy^1$ | GSD | 4.43 | −10.17 | | YK-Z-114 | $Z_3dy^2$ | SD | 1.6 | −12.27 | |
| JS1-6-6\75 | $Z_3dy3$ | GSD | 2.4 | −11.06 | | YK-Z-56 | $Z_3dy^2$ | SD | 4.39 | −13.72 | 0.82 |
| JS1-6-44\75 | $Z_3dy3$ | FCD | 1.53 | −12.06 | | YK-Z-6 | $Z_3dy^2$ | SD | 3.55 | −12.84 | 0.74 |
| FD-Zd-26 | $Z_3dy^1$ | FCD | 0.99 | −11.19 | 0.75 | YK-Z-60 | $Z_3dy^2$ | SD | 4.09 | −13.68 | 1 |
| YK-Z-43 | $Z_3dy^1$ | FCD | 3.19 | −11.47 | | YK-Z-84 | $Z_3dy^2$ | SD | 2.56 | −12.48 | |
| YK-Z-53 | $Z_3dy^1$ | FCD | 3.85 | −11.8 | | TZd37-1 | $Z_3dy^2$ | SD | 1.94 | −12.18 | |
| YK-Z-125 | $Z_3dy^3$ | FCD | 0.45 | −11.35 | | SLZd1-25 | $Z_3dy^2$ | SD | 1.01 | −13.63 | |
| YK-Z-129 | $Z_3dy^3$ | FCD | 1.48 | −11.95 | 0.71 | SLZd1-35 | $Z_3dy^2$ | SD | 2.27 | −14.05 | |
| JS1-6-34\75 | $JS^1$-6-34\75 | FCD | 1.77 | −11.22 | | TZd20-1 | $Z_3dy^2$ | SD | 1.67 | −14.2 | |
| YK-Z-80 | $Z_3dy^1$ | CCD | 2.74 | −12.55 | 1 | TZd31-1 | $Z_3dy^2$ | SD | 1.66 | −14.39 | |
| YK-Z-74 | $Z_3dy^1$ | CCD | 3.03 | −12.41 | 0.43 | DS1-10 9/44 | $Z_3dy^3$ | SD | 0.88 | −14.43 | |
| YK-Z-105 | $Z_3dy^1$ | CCD | 1.94 | −11.51 | | TZd36-1 | $Z_3dy^2$ | SD | 1.99 | −14.28 | |
| YK-Z-38 | $Z_3dy^1$ | CCD | 4.93 | −12.68 | | TZd7-2 | $Z_3dy^2$ | SD | 1.51 | −11.16 | |
| YK-Z-86 | $Z_3dy^1$ | CCD | 2.7 | −12.15 | 0.8 | | | | | | |

Note: FD, Fibrous dolomite; BD, Bladed dolomite; GSD, Granular sparry dolomite; FCD, Finely crystalline dolomite; MCD, Medium-coarse crystalline dolomite; CCD, Coarse crystalline dolomite; SD, Saddle dolomite.

0.85 to 0.90 (average 0.88) (Table 3), and REEs have a low degree of enrichment that is similar to dolomicrite (Fig. 7b).

**Finely crystalline dolomite.** The $\delta^{18}O$ values range from −11.95‰ to −10.17‰ PDB and are significantly different from those of the matrix. The $\delta^{13}C$ values fluctuate between 0.45‰ and 4.43‰ PDB (Fig. 8), order-degree values range from 0.60 to 0.75 (average 0.67) (Table 3), and REEs have a low degree of enrichment that is similar to dolomicrite (Fig. 7b).

**Coarsely crystalline dolomite.** The $\delta^{18}O$ values range from −13.32‰ to −8.95‰ PDB (average −11.56‰), $\delta^{13}C$ values range from 1.61‰ to 4.96‰ PDB (average 2.73‰) (Fig. 8), order-degree values are high and fluctuate between 0.50 and 1.00 (average 0.80%) (Table 3), and REEs suggest a low Eu positive anomaly and regular Ce content (Fig. 7b).

**Saddle dolomite.** The $\delta^{18}O$ values range from −12.48‰ to −15.12‰ PDB, with an average value of −13.53‰ PDB (Fig. 8), order-degree values range from 0.57 to 1 (average 0.83) (Table 3), REEs indicate a negative Ce anomaly and positive Eu anomaly (Fig. 7b), which is consistent with previous results (Wang Lichao et al., 2014).

### 4.3 Fluid inclusions

Fluid inclusion data are summarized in Table 4. Variations within dolomites suggest differences in the precipitation phases of fluids and their properties. Statistics of different types of mineral inclusions reveal several peaks in homogenization temperatures (Fig. 9a), particularly at temperature intervals of 130–145°C, 178–190°C, and 200–215°C. When our results are combined with those of a previous study on the hydrocarbon generation history of the Dengying Formation (Yuan Haifeng et al., 2014), these temperature intervals are found to be consistent with the homogenization temperature of crude oil expulsion, maturation, and cracking.

As the large number of organic inclusions was charged at a late stage, they could not be used in calculations to distinguish the original diagenetic fluids of dolomite minerals. Therefore, to obtain accurate temperatures for the dolomite fluid inclusions, the homogenization temperatures of organic inclusions and late-stage hydrothermal fluid inclusions were removed according to the principle that "late-stage fluids may form inclusions in early-stage minerals," and the homogenization temperature of each dolomite fluid inclusion was then obtained (Fig. 9b). Based on a previous analysis of hydrocarbon migration timing (Xu Guosheng et al., 2007), this study then obtained age-temperature curves of Dengying Formation dolomite and its associated minerals by analyzing relative mineral paragenesis and measured fluid inclusion data. A trend line was subsequently drawn to reflect the change trend of dolomite inclusion homogenization temperatures (Fig. 9c).

**Table 4 Fluid inclusion data of cement dolomites in Dengying Formation, Sichuan Basin**

| Sample No. | Lithology | Occurrence | Inclusion types | Size (mm) | gas/liquid ratio (%) | Phase | $T_h$ (°C) | Salinity (wt%NaCl) | Sample No. | Lithology | Occurrence | Inclusion types | Size (mm) | gas/liquid ratio (%) | Phase | $T_h$ (°C) | Salinity (wt%NaCl) |
|---|---|---|---|---|---|---|---|---|---|---|---|---|---|---|---|---|---|
| S-1 | SD | Fractures and vugs | Saline | 7×15 | ≤5% | Liquidus | 82.8 | Null | C-19 | CCD | Karst cave | Hydrocarbon | 10×8 | ≤5% | liquidus | 184 | 15.5 |
| S-2 | SD | Fractures and vugs | Saline | 5×10 | ≤5% | liquidus | 85 | Null | C-20 | CCD | Karst cave | Hydrocarbon | 6×8 | ≤5% | liquidus | 185 | 16.8 |
| S-3 | SD | Fractures and vugs | Saline | 4×18 | ≤5% | liquidus | 137.9 | Null | C-21 | CCD | Karst cave | Hydrocarbon | 12×10 | ≤5% | liquidus | 188 | 15.4 |
| S-4 | SD | Fractures and vugs | Saline | 8×15 | ≤5% | liquidus | 87.3 | Null | C-22 | CCD | Karst cave | Hydrocarbon | 8×10 | ≤5% | liquidus | 185 | 16.65 |
| S-5 | SD | Fractures and vugs | Saline | 15×20 | ≤5% | liquidus | 106.9 | Null | C-23 | CCD | Karst cave | Hydrocarbon | 10×13 | ≤5% | liquidus | 185 | 16.2 |
| S-6 | SD | Fractures and vugs | Saline | 9×18 | ≤5% | liquidus | 103.4 | Null | C-24 | CCD | Karst cave | Hydrocarbon | 6×30 | ≤5% | liquidus | 185 | 9.7 |
| S-7 | SD | Fractures and vugs | Saline | 13×30 | ≤5% | liquidus | 96.7 | Null | C-25 | CCD | Karst cave | Hydrocarbon | 16×30 | ≤5% | liquidus | 181 | 9.7 |
| S-8 | SD | Fractures and vugs | Saline | 14×18 | ≤5% | liquidus | 82.1 | Null | C-26 | CCD | Karst cave | Hydrocarbon | 8×20 | ≤5% | liquidus | 149 | 16.05 |
| S-9 | SD | Fractures and vugs | Saline | 6×12 | ≤5% | liquidus | 80.6 | Null | C-27 | CCD | Karst cave | Saline | 16×30 | ≤5% | liquidus | 155 | 7.91 |
| S-10 | SD | Fractures and vugs | Saline | 14×19 | ≤5% | liquidus | 90.3 | Null | C-28 | CCD | Karst cave | Saline | 9×13 | ≤5% | liquidus | 164 | 8.88 |
| S-11 | SD | Fractures and vugs | Saline | 14×28 | ≤5% | liquidus | 79.2 | Null | C-29 | CCD | Karst cave | Saline | 6×9 | ≤5% | liquidus | 156 | 8.95 |
| S-12 | SD | Fractures and vugs | Saline | 19×25 | ≤5% | liquidus | 91.9 | Null | C-30 | CCD | Karst cave | Saline | 4×9 | ≤5% | liquidus | 164 | 8.4 |
| S-13 | SD | Fractures and vugs | Saline | 14×20 | ≤5% | liquidus | 79.2 | Null | C-31 | CCD | Karst cave | Saline | 9×12 | ≤5% | liquidus | 155 | 9.25 |
| S-14 | SD | Fractures and vugs | Saline | 17×22 | ≤5% | liquidus | 107.8 | Null | C-32 | CCD | Karst cave | Saline | 10×12 | ≤5% | liquidus | 157 | 14.14 |
| S-15 | SD | Fractures and vugs | Saline | 12×18 | ≤5% | liquidus | 89.5 | Null | C-1 | CCD | Karst cave | Saline | 15×17 | ≤5% | liquidus | 153 | 12.02 |
| S-16 | SD | Fractures and vugs | Saline | 12×19 | ≤5% | liquidus | 99.2 | Null | C-2 | CCD | Karst cave | Hydrocarbon | 7×8 | ≤5% | liquidus | 142 | 10.25 |
| S-17 | SD | Fractures and vugs | Saline | 8×10 | ≤5% | liquidus | 73.3 | Null | C-3 | CCD | Karst cave | Hydrocarbon | 10×8 | ≤5% | liquidus | 148 | 10.5 |
| S-18 | SD | Fractures and vugs | Saline | 7×8 | ≤5% | liquidus | 82.1 | Null | C-4 | CCD | Karst cave | Saline | 6×8 | ≤5% | liquidus | 152 | 13.25 |
| S-19 | SD | Fractures and vugs | Saline | 10×8 | ≤5% | liquidus | 77.8 | Null | C-5 | CCD | Karst cave | Saline | 10×18 | ≤5% | liquidus | 160 | 13.7 |
| S-20 | SD | Fractures and vugs | Saline | 6×8 | ≤5% | liquidus | 66.5 | Null | C-6 | CCD | Karst cave | Saline | 8×10 | ≤5% | liquidus | 178 | 12.57 |
| S-21 | SD | Fractures and vugs | Saline | 10×18 | ≤5% | liquidus | 69 | Null | C-7 | CCD | Karst cave | Saline | 10×16 | ≤5% | liquidus | 169 | 12.12 |
| S-22 | SD | Fractures and vugs | Saline | 8×10 | ≤5% | liquidus | 76.4 | Null | C-8 | CCD | Karst cave | Saline | 9×20 | ≤5% | liquidus | 175 | 10.84 |
| S-23 | SD | Fractures and vugs | Saline | 10×16 | ≤5% | liquidus | 77.1 | Null | C-9 | CCD | Karst cave | Saline | 10×15 | ≤5% | liquidus | 167 | 10.55 |
| S-24 | SD | Fractures and vugs | Saline | 9×20 | ≤5% | liquidus | 82.1 | Null | C-10 | CCD | Karst cave | Saline | 10×15 | ≤5% | liquidus | 150 | 12.46 |
| S-25 | SD | Fractures and vugs | Saline | 10×15 | ≤5% | liquidus | 72.3 | Null | C-11 | CCD | Karst cave | Saline | 10×8 | ≤5% | liquidus | 164 | 13.14 |
| F-1 | FCD | Structural fracture | Saline | 6×9 | ≤5% | liquidus | 130 | 14.3 | C-12 | CCD | Karst cave | Saline | 5×15 | ≤5% | liquidus | 155 | 10.01 |
| F-2 | FCD | Structural fracture | Saline | 11×18 | ≤5% | liquidus | 136 | 14.3 | C-13 | CCD | Karst cave | Saline | 11×15 | ≤5% | liquidus | 163 | 10.66 |
| F-3 | FCD | Structural fracture | Saline | 4×9 | ≤5% | liquidus | 137 | 10.2 | C-14 | CCD | Karst cave | Saline | 8×10 | ≤5% | liquidus | 158 | 10 |
| F-4 | FCD | Structural fracture | Saline | 4×9 | ≤5% | liquidus | 137 | 12.8 | C-15 | CCD | Karst cave | Saline | 10×22 | ≤5% | liquidus | 168 | 8.68 |
| F-5 | FCD | Structural fracture | Saline | 5×10 | ≤5% | liquidus | 140 | 13 | C-16 | CCD | Karst cave | Saline | 7×23 | ≤5% | liquidus | 172 | 9.59 |
| F-6 | FCD | Structural fracture | Hydrocarbon | 4×18 | ≤5% | liquidus | 141 | 12.1 | C-17 | CCD | Karst cave | Hydrocarbon | 15×30 | ≤5% | liquidus | 183 | 15.5 |
| F-7 | FCD | Structural fracture | Hydrocarbon | 4×18 | ≤5% | liquidus | 141 | 12.5 | C-18 | CCD | Karst cave | Hydrocarbon | 9×19 | ≤5% | liquidus | 166 | 13.8 |
| F-8 | FCD | Structural fracture | Hydrocarbon | 15×19 | ≤5% | liquidus | 149 | 15 | C-19 | CCD | Karst cave | Saline | 12×20 | ≤5% | liquidus | 175 | 10.56 |
| F-9 | FCD | Structural fracture | Hydrocarbon | 15×10 | ≤5% | liquidus | 150 | 15.2 | C-20 | CCD | Karst cave | Hydrocarbon | 10×8 | ≤5% | liquidus | 187 | 14.5 |
| F-10 | FCD | Structural fracture | Hydrocarbon | 20×24 | ≤5% | liquidus | 150 | 15.5 | C-21 | CCD | Karst cave | Hydrocarbon | 6×8 | ≤5% | liquidus | 193 | 16.8 |
| F-11 | FCD | Structural fracture | Hydrocarbon | 12×18 | ≤5% | liquidus | 150 | 14.8 | C-22 | CCD | Karst cave | Hydrocarbon | 5×10 | ≤5% | liquidus | 195 | 14.24 |
| F-12 | FCD | Structural fracture | Hydrocarbon | 13×25 | ≤5% | liquidus | 155 | 16 | C-23 | CCD | Karst cave | Hydrocarbon | 8×10 | ≤5% | liquidus | 197 | 15.31 |
| F-13 | FCD | Structural fracture | Hydrocarbon | 8×12 | ≤5% | liquidus | 155 | 16.5 | C-24 | CCD | Karst cave | Hydrocarbon | 10×13 | ≤5% | liquidus | 194 | 17.71 |
| F-14 | FCD | Structural fracture | Hydrocarbon | 9×14 | ≤5% | liquidus | 155 | 18 | C-25 | CCD | Karst cave | Hydrocarbon | 6×12 | ≤5% | liquidus | 117 | 10.22 |
| F-15 | FCD | Structural fracture | Hydrocarbon | 4×9 | ≤5% | liquidus | 159 | Null | C-26 | CCD | Karst cave | Hydrocarbon | 6×9 | ≤5% | liquidus | 120 | 10.76 |
| F-16 | FCD | Structural fracture | Hydrocarbon | 3×10 | ≤5% | liquidus | 159 | Null | C-27 | CCD | Karst cave | Hydrocarbon | 5×12 | ≤5% | liquidus | 109 | 10 |
| F-17 | FCD | Structural fracture | Hydrocarbon | 5×8 | ≤5% | liquidus | 159 | Null | C-28 | CCD | Karst cave | Hydrocarbon | 9×12 | ≤5% | liquidus | 112 | 12.13 |
| F-18 | FCD | Structural fracture | Hydrocarbon | 6×22 | ≤5% | liquidus | 161 | 14.3 | C-29 | CCD | Karst cave | Saline | 6×13 | ≤5% | liquidus | 155 | 10.1 |
| F-19 | FCD | Structural fracture | Hydrocarbon | 8×9 | ≤5% | liquidus | 161 | 19.2 | C-30 | CCD | Karst cave | Saline | 9×18 | ≤5% | liquidus | 167 | 13.6 |
| F-20 | FCD | Structural fracture | Hydrocarbon | 4×13 | ≤5% | liquidus | 161 | 18.95 | C-31 | CCD | Karst cave | Saline | 10×16 | ≤5% | liquidus | 165 | 13.85 |
| F-21 | FCD | Structural fracture | Hydrocarbon | 19×25 | ≤5% | liquidus | 168 | 19.3 | C-32 | CCD | Karst cave | Saline | 6×10 | ≤5% | liquidus | 150 | 11.86 |
| F-22 | FCD | Structural fracture | Hydrocarbon | 19×22 | ≤5% | liquidus | 170 | 18.1 | C-33 | CCD | Karst cave | Saline | 5×23 | ≤5% | liquidus | 159 | 12 |

**Table 4 Continued**

| Sample No. | Lithology | Occurrence | Inclusion types | Size (mm) | gas/liquid ratio (%) | Phase | $T_h$ (°C) | Salinity (wt%NaCl) |
|---|---|---|---|---|---|---|---|---|
| F-23 | FCD | Dissolved fracture | Hydrocarbon | 20×24 | ≤5% | liquidus | 145 | 19.8 |
| F-24 | FCD | Dissolution fracture | Hydrocarbon | 4×7 | ≤5% | liquidus | 141 | Null |
| F-25 | FCD | Dissolution fracture | Saline | 4×7 | ≤5% | liquidus | 140 | Null |
| F-26 | FCD | Dissolution fracture | Saline | 5×9 | ≤5% | liquidus | 120 | 19.8 |
| F-27 | FCD | Dissolution fracture | Saline | 3×10 | ≤5% | liquidus | 124 | 14 |
| F-28 | FCD | Dissolution fracture | Saline | 4×8 | ≤5% | liquidus | 127 | 14.1 |
| F-29 | FCD | Dissolution fracture | Hydrocarbon | 10×8 | ≤5% | liquidus | 143 | 13.3 |
| F-30 | FCD | Dissolution fracture | Hydrocarbon | 9×13 | ≤5% | liquidus | 149 | 13 |
| F-31 | FCD | Dissolution fracture | Hydrocarbon | 12×12 | ≤5% | liquidus | 144 | 12.9 |
| F-32 | FCD | Dissolution fracture | Saline | 4×9 | ≤5% | liquidus | 140 | 12.5 |
| F-33 | FCD | Dissolution fracture | Hydrocarbon | 5×9 | ≤5% | liquidus | 142 | 13 |
| F-34 | FCD | Karst cave | Saline | 4×10 | ≤5% | liquidus | 132 | 13.6 |
| F-35 | FCD | Karst cave | Saline | 4×12 | ≤5% | liquidus | 135 | 13.4 |
| F-36 | FCD | Karst cave | Saline | 6×11 | ≤5% | liquidus | 130 | 11.6 |
| F-37 | FCD | Karst cave | Saline | 5×15 | ≤5% | liquidus | 138 | 11.5 |
| F-38 | FCD | Karst cave | Saline | 5×10 | ≤5% | liquidus | 140 | 12 |
| F-39 | FCD | Karst cave | Saline | 4×11 | ≤5% | liquidus | 133 | 11.4 |
| C-1 | CCD | Karst cave | Hydrocarbon | 10×15 | ≤5% | liquidus | 199.5 | 18.2 |
| C-2 | CCD | Karst cave | Hydrocarbon | 20×24 | ≤5% | liquidus | 209 | 18.8 |
| C-3 | CCD | Karst cave | Hydrocarbon | 12×18 | ≤5% | liquidus | 200 | 18.5 |
| C-4 | CCD | Karst cave | Hydrocarbon | 13×25 | ≤5% | liquidus | 200 | 19 |
| C-5 | CCD | Karst cave | Hydrocarbon | 11×17 | ≤5% | liquidus | 231 | 19.1 |
| C-6 | CCD | Karst cave | Saline | 6×11 | ≤5% | liquidus | 175 | 13.95 |
| C-7 | CCD | Karst cave | Hydrocarbon | 13×17 | ≤5% | liquidus | 187 | 16.5 |
| C-8 | CCD | Karst cave | Hydrocarbon | 24×36 | ≤5% | liquidus | 185 | 16.1 |
| C-9 | CCD | Karst cave | Hydrocarbon | 20×25 | ≤5% | liquidus | 186 | 15.98 |
| C-10 | CCD | Karst cave | Hydrocarbon | 14×19 | ≤5% | liquidus | 185 | 16.12 |
| C-11 | CCD | Karst cave | Hydrocarbon | 17×18 | ≤5% | liquidus | 185 | 15.98 |
| C-12 | CCD | Karst cave | Hydrocarbon | 15×18 | ≤5% | liquidus | 185 | 15.75 |
| C-13 | CCD | Karst cave | Hydrocarbon | 12×16 | ≤5% | liquidus | 183 | 16.05 |
| C-14 | CCD | Karst cave | Hydrocarbon | 8×10 | ≤5% | liquidus | 184 | 16.5 |
| C-15 | CCD | Karst cave | Hydrocarbon | 10×15 | ≤5% | liquidus | 185 | 7.85 |
| C-16 | CCD | Karst cave | Hydrocarbon | 10×30 | ≤5% | liquidus | 185 | 9.7 |
| C-17 | CCD | Karst cave | Hydrocarbon | 10×15 | ≤5% | liquidus | 185 | 12.89 |
| C-18 | CCD | Karst cave | Hydrocarbon | 12×14 | ≤5% | liquidus | 186 | 16.05 |

| Sample No. | Lithology | Occurrence | Inclusion types | Size (mm) | gas/liquid ratio (%) | Phase | $T_h$ (°C) | Salinity (wt%NaCl) |
|---|---|---|---|---|---|---|---|---|
| C-34 | CCD | Karst cave | Saline | 6×20 | ≤5% | liquidus | 169 | 14.01 |
| C-35 | CCD | Karst cave | Hydrocarbon | 5×15 | ≤5% | liquidus | 149 | 10.1 |
| C-36 | CCD | Karst cave | Saline | 9×18 | ≤5% | liquidus | 158 | 14 |
| S-1 | SD | Karst cave | Saline | 8×16 | ≤5% | liquidus | 253 | 15 |
| S-2 | SD | Karst cave | Saline | 8×21 | ≤5% | liquidus | 258 | 18.8 |
| S-3 | SD | Karst cave | Saline | 9×15 | ≤5% | liquidus | 258 | 15.2 |
| S-4 | SD | Karst cave | Saline | 11×20 | ≤5% | liquidus | 260 | 15.52 |
| S-5 | SD | Karst cave | Saline | 10×8 | ≤5% | liquidus | 248 | 16.01 |
| S-6 | SD | Karst cave | Saline | 5×15 | ≤5% | liquidus | 244 | 16.2 |
| S-7 | SD | Karst cave | Saline | 9×16 | ≤5% | liquidus | 248 | 16.05 |
| S-8 | SD | Karst cave | Saline | 8×18 | ≤5% | liquidus | 260 | 16.07 |
| S-9 | SD | Karst cave | Saline | 7×16 | ≤5% | liquidus | 250 | 15 |
| S-10 | SD | Karst cave | Saline | 6×22 | ≤5% | liquidus | 247 | 16.05 |
| S-11 | SD | Karst cave | Saline | 15×30 | ≤5% | liquidus | 251 | 15.5 |
| S-12 | SD | Karst cave | Saline | 8×18 | ≤5% | liquidus | 260 | 15.8 |
| S-13 | SD | Karst cave | Saline | 12×22 | ≤5% | liquidus | 258 | 15 |
| S-14 | SD | Karst cave | Saline | 6×8 | ≤5% | liquidus | 250 | 15 |
| S-15 | SD | Karst cave | Saline | 8×18 | ≤5% | liquidus | 255 | 16.05 |
| S-16 | SD | Karst cave | Saline | 7×10 | ≤5% | liquidus | 258 | 15 |
| S-17 | SD | Karst cave | Saline | 8×20 | ≤5% | liquidus | 261 | 15.01 |
| S-18 | SD | Karst cave | Saline | 6×15 | ≤5% | liquidus | 258 | 15 |
| S-19 | SD | Karst cave | Saline | 11×16 | ≤5% | liquidus | 258 | 15.46 |
| S-20 | SD | Karst cave | Saline | 8×16 | ≤5% | liquidus | 258 | 15.6 |
| S-21 | SD | Karst cave | Saline | 7×13 | ≤5% | liquidus | 258 | 15.87 |
| S-22 | SD | Karst cave | Saline | 5×15 | ≤5% | liquidus | 258 | 15.35 |
| S-23 | SD | Karst cave | Saline | 10×16 | ≤5% | liquidus | 258 | 15.9 |
| S-24 | SD | Karst cave | Saline | 8×10 | ≤5% | liquidus | 258 | 15.55 |
| S-25 | SD | Karst cave | Saline | 11×20 | ≤5% | liquidus | 258 | 15.77 |
| S-26 | SD | Karst cave | Saline | 6×22 | ≤5% | liquidus | 258 | 16.01 |
| S-27 | SD | Karst cave | Saline | 12×25 | ≤5% | liquidus | 257 | 15.99 |
| S-28 | SD | Karst cave | Saline | 8×19 | ≤5% | liquidus | 250 | 15.32 |
| S-29 | SD | Karst cave | Saline | 10×21 | ≤5% | liquidus | 250 | 15.65 |
| S-30 | SD | Karst cave | Saline | 10×18 | ≤5% | liquidus | 248 | 15.23 |
| S-31 | SD | Karst cave | Saline | 6×8 | ≤5% | liquidus | 249 | 15.7 |

Note: SD, Siliceous dolomite; FCD, Finely crystalline dolomite; CCD, Coarse crystalline dolomite; SD, Saddle dolomite.

The homogenization temperatures of inclusions in most minerals show linearly increasing trends, which indicates that they were not controlled by geothermal gradient changes. In addition, the homogenization temperature ($T_m$) values of fluid inclusions corresponding to two periods of hydrocarbon migration are consistent with our trend line. As it was previously proposed that the result from the buried heating effect (Yuan Haifeng et al., 2014), and thus the $T_m$ values, should be closely related to the geothermal gradient, the inclusion temperatures determined here are not abnormal, and in this respect the validity of the trend line is indirectly demonstrated. However, the $T_m$ values of inclusions in saddle dolomite and bladed quartz are abnormal, implying that inclusions in saddle dolomite and bladed quartz were formed from external fluids.

## 5 Discussions

### 5.1 Origin of fluids

Different types of geological fluids form during the diagenetic process of minerals, and mineral elements migrate (Urey et al., 1947, 1948). Based on previous fluid studies and empirical data (Stein et al., 2000; Korte et al., 2006), the geochemical data of minerals in the study area were inverted to reconstruct diagenetic fluid characteristics. Primary inclusions have a special crystalline structure and are rarely found in fibrous dolomites; few data therefore exist on the $T_m$ values of their
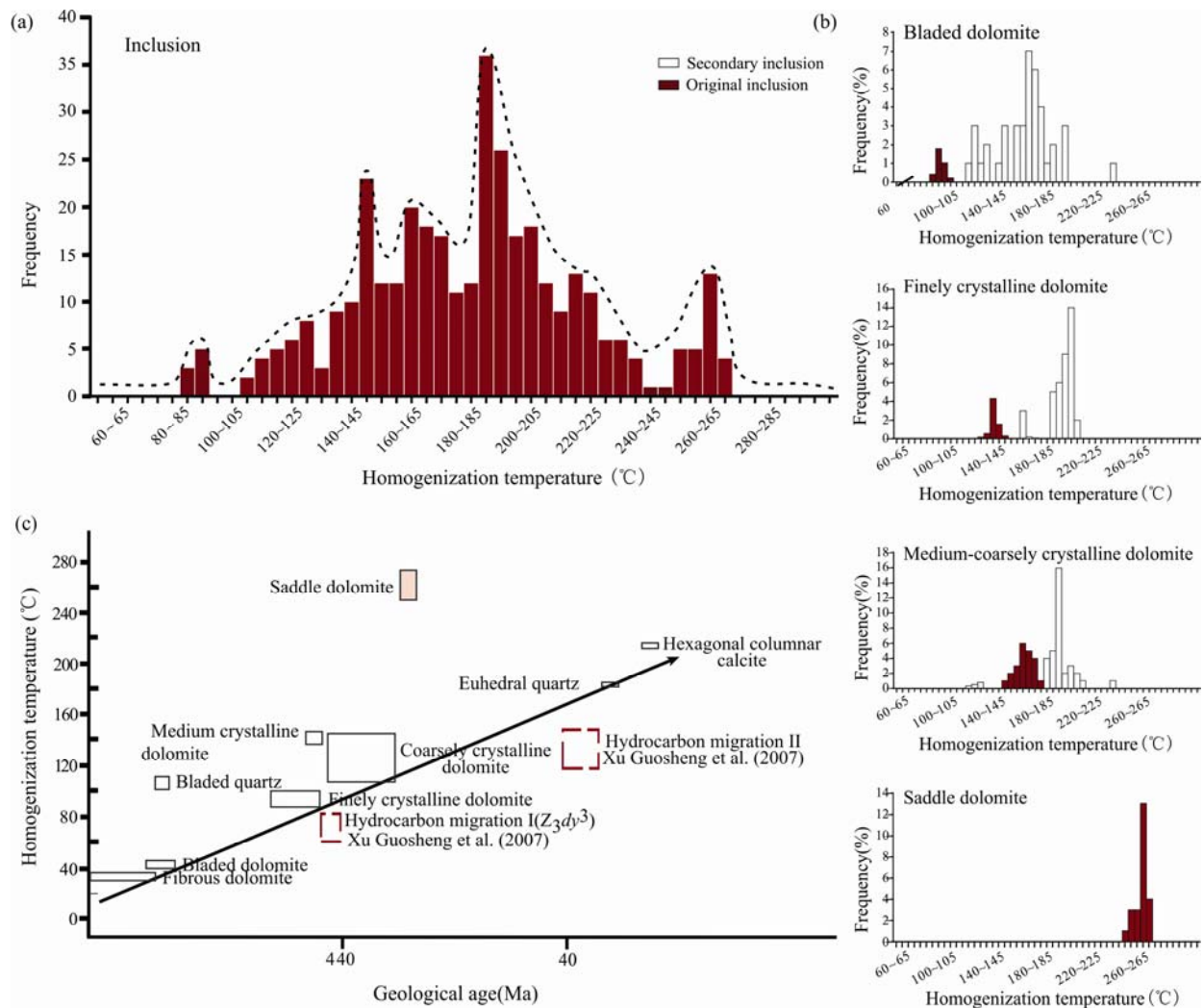
Fig. 9. Homogenization temperature analysis chart of fluid inclusions in Precambrian Dengying Formation dolomite and associated minerals.

(a), Homogenization temperature statistics for multi-phase fluid inclusions of Dengying Formation; inclusions with temperatures from 178–190°C have the highest frequency and represent the large amounts of organic inclusions after crude oil cracking; (b), Homogenization temperature of inclusions in dolomite fillings. Homogenization temperature of inclusions in bladed dolomite $T$ (°C), grape-like dolomite, and blade dolomite were formed at an earlier stage, multi-phase fluid inclusions co-existed, and the red area represents secondary inclusions. Homogenization temperature of inclusions in finely crystalline dolomite in fractures and vugs $T$ (°C) formed at an earlier stage, multi-phase fluid inclusions co-existed, and the red area represents secondary inclusions. Homogenization temperature of inclusions in moderate-to-coarse crystalline dolomite in fractures and vugs $T$ (°C) was between 145 °C and 175 °C, and a large amount of liquid-gaseous hydrocarbon inclusions existed after closure to the oil and gas cracking stage. Homogenization temperature of inclusions in saddle dolomite $T$ (°C), saddle dolomite in fractures and vugs was formed at a later stage in the diagenetic sequence, so that secondary inclusions are rare and inclusion temperature is concentrated; (c), Age- temperature curves of Dengying Formation dolomite and its associated minerals. Trend line represents variation trend in $T_m$ values of fluid inclusions in different minerals with time, and the mineral order is consistent with the diagenetic sequence.

fluid inclusions. Fibrous dolomites represent the first dolomite phase in syngenetic algal window-shaped holes, and it is thus indicated that they were precipitated by earlier fluids. It has been argued that dolomites were transformed from the dolomitization of aragonite and magnesium calcite (Huang Sijing et al., 2010), and the fibrous structure has also been found in modern sea water cement, which thus indicates that they may have been precipitated during the penecontemporaneous to shallow burial period. Geochemical data have identified that these fibrous dolomites share similar characteristics with matrix dolomites with respect to their cathodoluminescence

characteristics and stable isotope features. In addition, the fluid temperatures of fibrous dolomites are similar to those of temperatures at that time, 40.8°C (Huang Zhicheng et al., 1999), and the $\delta^{18}O$ values of diagenetic fluids, calculated from Formula 1(Land et al., 1967, 1980), vary from -2.84 to 0.44‰ SMOW, which are within the seawater $\delta^{18}O$ range (Faure et al., 1977),

$$1000\ln\alpha \text{ (dolomite-water)} = 3.14\prime10^6T^{-2}-2.0 \qquad (1)$$

The granular dolosparite and bladed dolomites that filled-in window-like pores are syngenetic dolomite cements, which were easily affected by late-stage diagenetic fluids; therefore, the homogenization

temperature curves of fluid inclusions represent multimodal morphologies. Bladed dolomite has a similar paragenesis to that of hydrothermal siliceous matter of the syngenetic stage and the OM of the first phase; it was thus significantly influenced by secondary inclusions of submarine siliceous hydrothermal fluids ($T_h$ values about 100°C) and oil and gas inclusions were expulsed in the first phase ($T_h$ values of 115 to 140 °C) (Yuan Haifeng et al., 2014). The $T_h$ values of acquired primary inclusions are similar to that of seawater temperature (approximately 40.8°C). The $\delta^{18}O$ values of diagenetic fluids, calculated using Formula 1, range from −12.83‰ to −11.54‰ SMOW (Formula 1), indicating that granular dolosparite was precipitated by a fluid related to meteoric freshwater (Fig. 10a). The $\delta^{18}O$ values of bladed dolomite fluids range from −0.18‰ to 0.42‰ SMOW (Fig. 10b), which is consistent with the range in seawater (Faure et al., 1977).

Finely crystalline dolomite was precipitated slightly earlier than first-phase asphalt. With the influence of secondary inclusions from Hydrocarbon migration I, the inclusion homogenization temperature curves present a bimodal shape. Primary inclusions yield $T_h$ values of 130–140°C, $\delta^{18}O$ values of −11.95‰ to −10.17‰ PDB; and the $\delta^{18}O$ values of diagenetic fluids, calculated from Formula 1, vary from −0.24‰ to 4.14‰ SMOW, which is between the ranges of seawater and formation water (Fig. 10c). The inclusion Tm values are concentrated from −10 to −7°C; salinity levels calculated from $T_m$ values (Lu Huanzhang et al., 2016) vary from 9.7%–14.3%, wt% NaCl equivalent. Electron probe microanalysis shows that the minerals are rich in $Fe^{2+}$ (1.23 ppm) and $Mn^{2+}$ (0.089 ppm), which is significantly different from the host

carbonates. Results indicate that the finely crystalline dolomite was precipitated from a two-component fluid incorporating a significant quantity of seawater fluid and a brine with moderate-to-high salinity and high Fe and Mn concentrations, which imply a relatively restricted environment.

The paragenesis of moderate-coarse crystalline dolomite is later than that of organic hydrocarbon fluids of the first phase (115–140°C) and earlier than organic hydrocarbon fluids of the second phase (160–173°C) (Yuan Haifeng et al., 2014); therefore, a large number of fluid-gas hydrocarbon inclusions occurred during the pyrolysis period, resulting in the biomodal shapes of homogenization temperature curves of fluid inclusions. $T_h$ values range from 150–175°C with $\delta^{18}O$ values of −8.95‰ to −13.32‰ PDB. Fluids have $\delta^{18}O$ values from 1.44‰ to 5.37‰ (SMOW), which categorize them as interlayer fluids (Fig. 10d). Tm values of inclusions are concentrated at −5 to −10°C and converted to salinity as 7.85% to 14.05%. It can thus be inferred that the diagenetic fluid within coarsely crystalline dolomite is that of moderate-to-high salinity formation water.

The diagenetic stage of SD is later than that of other dolomites. The $T_m$ values of primary inclusions are concentrated, plot a single-peak curve, and are higher (250–265°C) than those of dolomite inclusions of the early stage (Wang Guozhi et al., 2009). The $\delta^{18}O$ values of saddle dolomite are 5.47‰ to 7.62‰ SMOW, which lie in the range of hydrothermal mineral genesis (Fig. 10e), and Tm values of inclusions are concentrated at −11 to −12°C, which are converted to salinity as 15% to 16.05%. It can thus be inferred that the diagenetic fluid of saddle
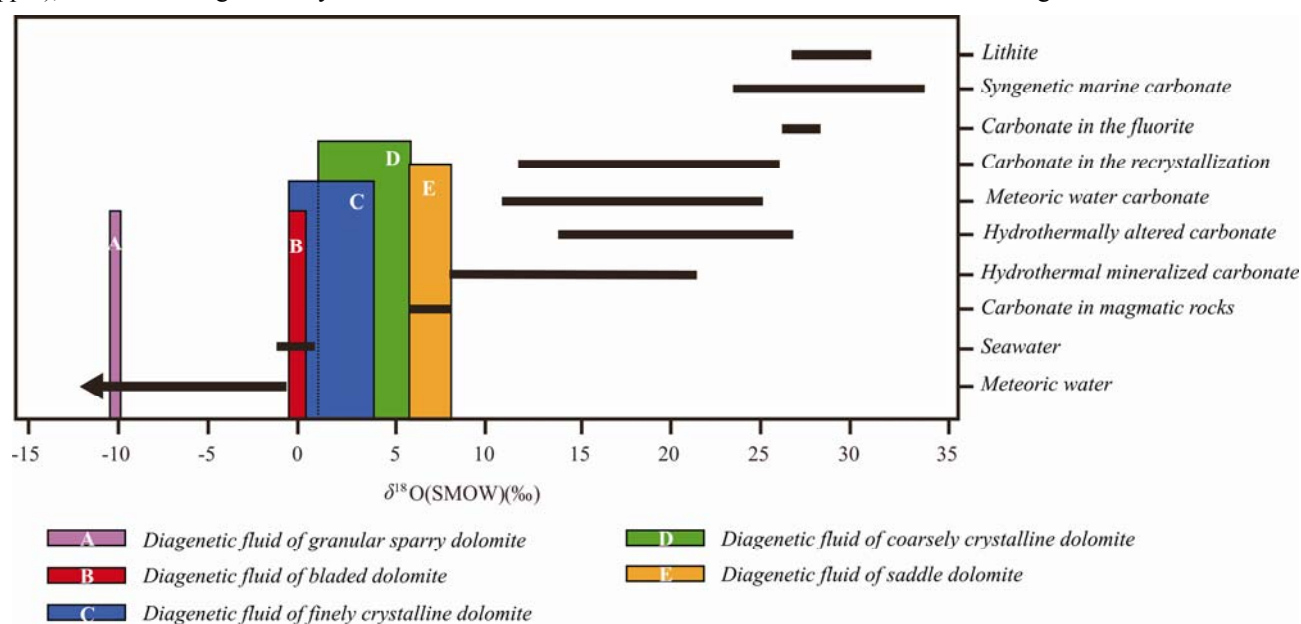


Fig. 10. $\delta^{18}O$ isotope characteristics of different fluids in Precambrian Dengying Formation dolomites in Sichuan Basin (collected data plotted in chart modified from Le Changshuo,1984 and Huang Sijing et al., 2010).

dolomite is that of high salinity hydrothermal fluids.

Based on the cross-plot of fluid inclusion homogenization temperatures and oxygen isotope data (Fig. 11), the $\delta^{18}O$ values of fluids (SMOW) are obtained at different values, thereby representing various fluid types. Geological fluids related to dolomites are generally varying types and formed in multiple phases. Overall, $\delta^{18}O$ values of dolomite fluids show an increasing trend from −12.83‰ to 9.20‰ SMOW, representing a transition from an early- to late-charging phase. According to the above analysis, it can be concluded that the fluid type evolved from seawater, successively transited toward meteoric freshwater and formation water, and finally into hydrothermal fluids.

## 5.2 Environmental indications from typical associated minerals

According to mineral formation stages, the associated minerals can be divided into four combinations.

The associated mineral combination of Stage I is mainly related to siliceous rocks, including micritic quartz, bladed quartz, chert, and opal, accompanied by dolomite siliceous metasomatism. The main homogenization temperature peaks of fluid inclusions are between 90.0 and 105.0°C (Ma Wenxin et al., 2011), which are extremely close to those of siliceous dolomites. Chen Daizhao et al. (2015) proposed that such siliceous rocks are related to the

penecontemporaneous seafloor hydrothermal chimney and their formation time is close to that of the sedimentary time.

The associated mineral combination of Stage II includes two stages of OM. Vitrinite reflectance and fluid inclusion data show that first-stage OM is characterized by a low homogenization temperature (65–89°C) and low maturity, while second-stage OM is characterized by a high homogenization temperature (120–173° C) and high maturity (Xu Guosheng et al., 2007). No other hydrothermal mineral fillings have been found, either before or after OM filling, which indicates that hydrocarbon generation may be related to an increase in the formation burial depth, temperature, and pressure. According to biomarkers, first- and second-stage OM are respectively related to $Z_3dy^2$ shales and Upper Niutitang Formation shales. The burial depths corresponding to two hydrocarbon expulsion periods are respectively 2100–2250 m (shallow-middle burial depth) and 4400–4600 m (deep burial depth), assuming the geothermal gradient in the area is 4°C/100 m.

The associated mineral combination of Stage III is related to hexagonal columnar calcite, and is generally associated with saddle dolomites and featured by high fluid inclusion homogenization temperatures varying from 202–251.5°C. Its homogenization temperature peak is 213.7–230°C, which is slightly lower than that of saddle dolomite.
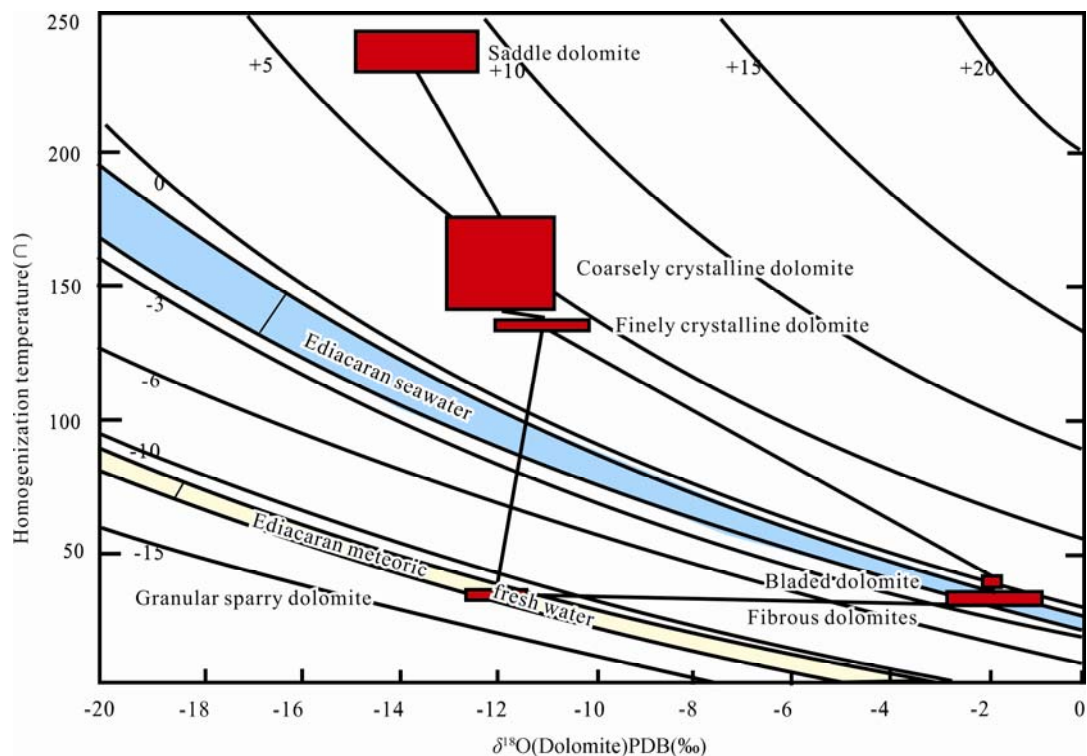


Fig. 11. Cross-plot of fluid inclusion homogenization temperature ($T_h$) and oxygen isotope of Precambrian Dengying Formation dolomite (Note: contour represents isotopic composition of water in isotope equilibrium state of dolomite).

However, the homogenization temperature is higher than the maximum Dengying Formation temperature, which indicates the hydrothermal origin of saddle dolomite(Peng Bo et al.,2018).

The associated mineral combination of Stage IV consists of fluorite, lead-zinc ore, celestite, euhedral granular quartz, and pyrite. Large amounts of hydrocarbon inclusions occur with homogenization temperatures varying from 180–200°C. Raman spectrum analysis show that cracked gas dominates in the hydrocarbon composition but there is limited liquid hydrocarbon in relation to hydrocarbon cracking. The cracked gas reservoir was destroyed by the Yanshanian Movement, and it is therefore not possible to find minerals that occurred during both the deep and shallow burial periods.

## 5.3 Fluid flow events

Studies have confirmed that precipitation of siliceous rocks in the Dengying Formation occurred in the Late Precambrian Ediacaran (630–542 Ma), and are related to the contemporaneous heterotopic facies of siliceous rocks of the Liuchapo Formation. Its zircon SHRIMP dating is 536.3±5.5 Ma (Chen Daizhao et al., 2015). It is known that the study area experienced two phases of hydrocarbon migration: the first phase occurred from the Late Ordovician to the Early Silurian (450–430 Ma). In the Late Silurian, the Caledonian Movement resulted in stratigraphic uplift and denudation, thereby terminating the first hydrocarbon migration period. The second hydrocarbon migration pattern then began after the Hercynian Movement (E'mei Taphrogeny) (250 Ma) (Xu Guosheng et al., 2013). With growing burial depth, oil and gas began to crack from rocks from the Late Triassic to Early Jurassic, but original gas accumulations were destroyed during the Late Jurassic-Early Cretaceous due to Yanshanian tectonic uplift (128–134 Ma), leading to enrichment of sphalerite, fluorite, and other heavy minerals (Wang Guozhi et al., 2013).

The major timing of dolomite fluid activities is approximately identified through an analysis of the relationship between typical associated dolomite and dolomite paragenesis, dating data of critical associated minerals, and the oil and gas charging history. The timing and Tm values of different types of dolomites can then be projected onto the burial history chart. The projection zone of homogenization temperatures was restricted to be no wider than the timing range of dolomite fluid activities, and the geological interpretation of the projection position was in accordance with understandings gained from studying the dolomite fluid properties. The final projection result is shown in Fig. 12.

## 5.4 Mechanism and models

Based on above analysis, the mineralization timing and dolomite formation mechanisms of in the Precambrian Dengying Formation within the central and southern Sichuan Basin, are discussed as follows (Table 5). Figure 13 presents a schematic diagram of the dolomite formation mechanism.

### 5.4.1 Stage one: Multi-phased geological fluids and associated control on dolomite distribution during depositional stage

The Upper Precambrian Dengying Formation was deposited during 630–542 Ma. At this time, the paleoclimate was warmer compared to the Early Precambrian Doushantuo Period, and the relative sea level began to rise until the Luding landmass was drawn, leading to a well-developed large epicontinental carbonate platform throughout most of the basin. In relation to the high temperature climate (paleo-fluid analysis shows that the seawater temperature reached 40.8°C at that time) (Huang Zhicheng et al., 1999), micritic dolomite, finely crystalline dolomite, and algae dolomicrite matrix were extensively precipitated under the impact of dolomitization of evaporated seawater. Geochemical data indicate that dolomitization characteristics varied throughout different facies belts. Dolomicrite precipitated in the supratidal zone has similar characteristics to the small amount of dolomicrite with algae adhesive structures, as they are both products of evaporative pumping dolomitization. In addition, dolomicrite with algae laminate and finely crystalline dolomite precipitated in the intertidal zone; these have similar geochemical characteristics and both are considered to be seepage reflux dolomitization products.

Fibrous dolomite and granular dolosparite were formed in the fractures and vugs of the syndiagenetic stage under the co-reworking of meteoric freshwater and seawater. These types of dolomite developed in the intertidal environment and are frequently exposed. Fractures and vugs were formed due to meteoric water leaching and exposure. Dolomite cemented in the walls of fractures and vugs formed fibrous dolomite under seawater action during a period of submergence, and has similar geochemical characteristics to seawater. When exposed, granular dolosparite has a negative $\delta^{18}O$ and is of a low-order degree under meteoric conditions. Short periodical exposure resulted in multiple sets of fibrous dolomite-granular dolosparite circle layers formed in large fractures and vugs (grape-like structure). However, residual spaces are generally filled with coarse-bladed dolomite.

During the late depositional period of the Dengying Formation, 536.3 ± 5.5 Ma, submarine hydrothermal
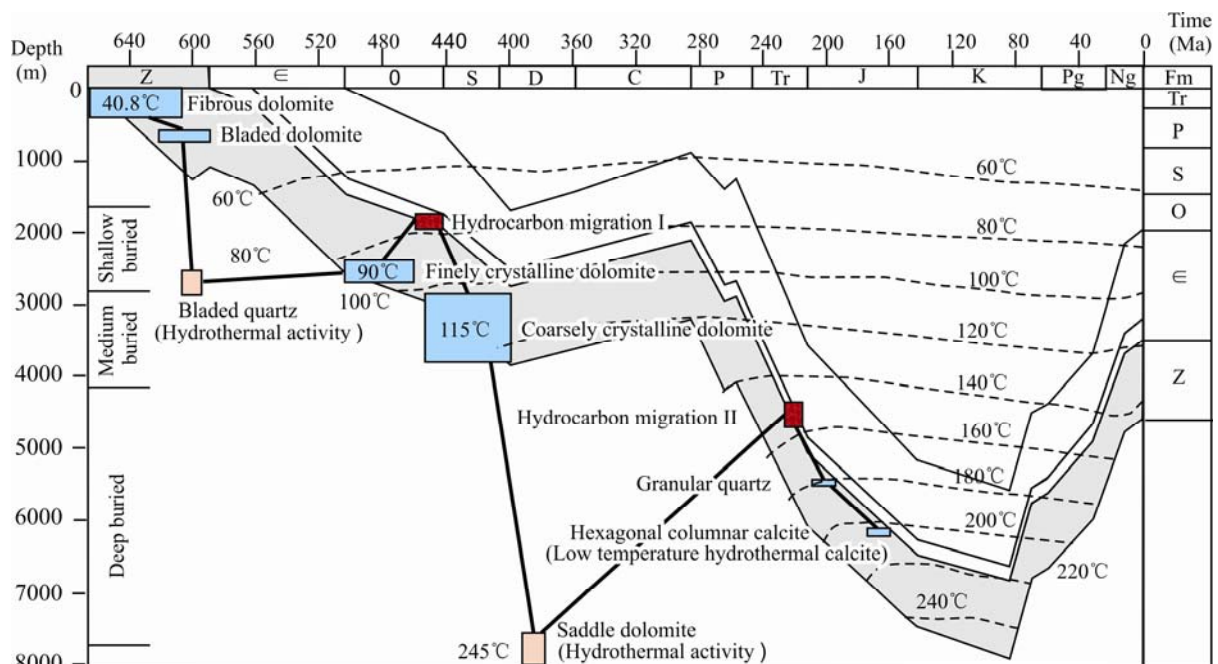
Fig. 12. Burial history chart and fluid temperature analysis of Precambrian Dengying Formation dolomite in southern Sichuan Basin.

**Table 5 Mineralization timing and dolomite formation mechanisms of Precambrian Dengying Formation dolomites in middle and southern Sichuan Basin**

| Diagenetic stage | Speculated time limit | Hydrocarbon generation stage | Fluid types | Environment | Mineral types | Dolomitization mode |
|---|---|---|---|---|---|---|
| Penecontemporaneous | 630–542 Ma | | Seawater | Open environment | Microcrystalline dolomite matrix | Evaporated seawater mode |
| | | | | | Algae micrite matrix dolomite | |
| | | | | | Finely crystalline matrix dolomite | |
| | | | | | Fibrous dolomite fractures and | |
| | | | | | Bladed dolomite | |
| | | | Meteoric | | Granular dolosparite | Mixed water mode |
| | 536.3±5. | | Submarine | | Siliceous dolomite | Hydrothermal |
| Early shallow | | | Formation water | | Finely crystalline dolomite in | Compaction mode |
| Middle | | Early | | Enclosed environment | | |
| Moderate-deep burial | | | Formation water | | Moderate-coarse-crystalline | Tectonic-driven |
| | 280–360 | | Magmatic | Semi-open | Saddle dolomite | Hydrothermal |
| | | | Liquid | Enclosed environment | | |
| Deep burial | 128–134 | Cracked gas | | | | |

fluids rich in siliceous component controlled the distribution of siliceous dolomite, and several large sets of hydrothermal siliceous dolomite were formed in the overlying strata of Dengying Formation. Some scholars believe these occurred extensively in the platform rift belt and on the platform margin.

### 5.4.2 Stage two: Geological fluid evolution and associated control on dolomite distribution during shallow burial stage

After Caledonian uplifting, burial of the Dengying Formation began. During this time, $Z_3dy^2$ source rocks entered the hydrocarbon generation threshold, and the environment changed from one that was semi-open to

being restricted. The fluids therefore changed from seawater into formation water. Under compaction, dolomites rich in Mg ions were accumulated in the fractures and vugs at an early stage, and dolomitization occurred extensively. FCDs filled in the fractures and vugs after first-stage OM filling. The transient burial duration resulted in small crystal sizes, which electron probe results reveal to have a high mineral content. Dolomite was distributed in the dissolution fractures and vugs of a syndiagenetic stage, and the surface of dissolution fractures and vugs of a late stage, but not in the window-like pores that are related to an algae structure.

### 5.4.3 Stage three: Geological fluid evolution and
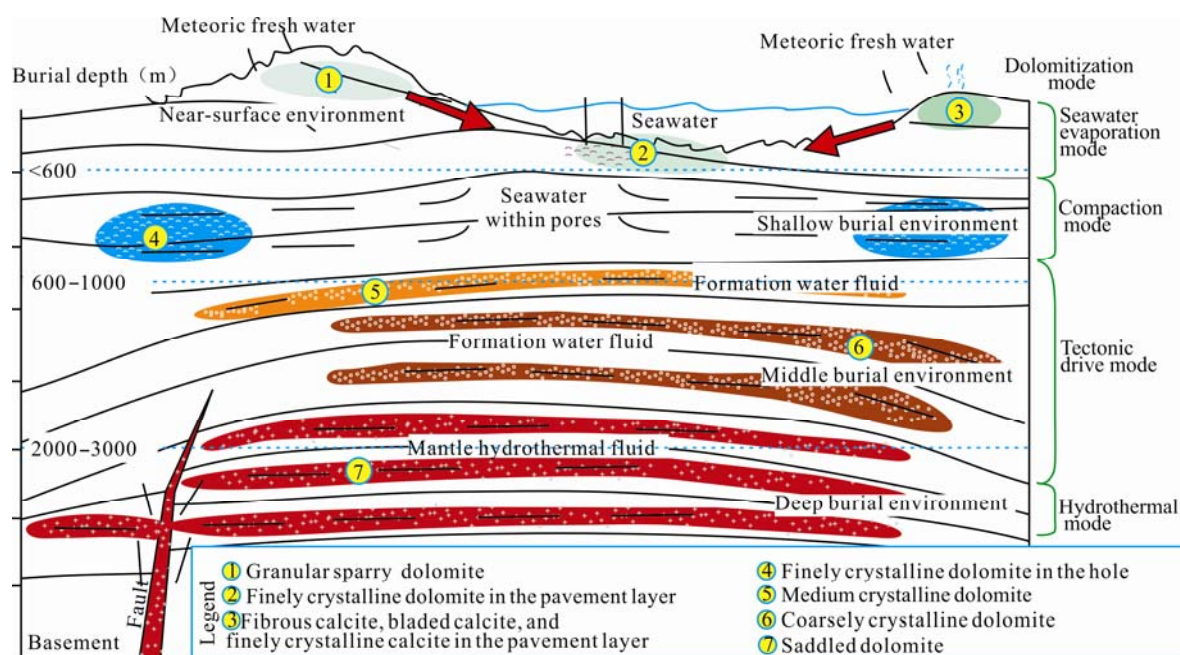
Fig. 13. Dolomitization mechanism occurring within Precambrian Dengying Formation in Sichuan Basin.

**associated control on dolomite distribution during moderate-deep burial stage**

With a deepening of the burial depth, middle-high salinity formation water began to dominate and produced middle to coarse euhedral dolomites. Fluid inclusion homogenization temperatures (150–175°C) were lower than those of the deep mantle, and so was the salinity of inclusions. Fluids with high homogenization temperatures may have originated from the buried heating effect, and with no large-scale tectonic extension, formation water occurred in a restricted environment at depths greater than 3000 m. The dolomite often filled-in encrustation type fractures and vugs, and epigenetic karst fractures and vugs formed due to the Tongwan Movement. In addition, the precipitation of dolomite was intensively influenced by tectonic stress during the burial stage, and its distribution related to the fluid low potential region in the late Caledonian.

During 280–360 Ma, the Caledonian Movement ended and the Hercynian Movement began. Tectonic stress in the study area altered from compressional to extensional. Intense extension resulted in hydrothermal fluid upwelling in the underlying strata and hydrothermal dolomitization, thereby forming SD, which was ultimately distributed throughout the entire region. Saddle dolomite mainly occurs in large dissolution fractures and vugs, and in the structural fractures of the late stage, where it generally cuts country rock or fills-in dissolution fractures of the early stage. The extension caused a transient open environment, as a large fault linked the surface to the deep part during the Hercynian. Hydrothermal fluid from the deep restricted mantle environment then partly mixed with small amounts of surface open environmental fluid, causing the abnormal geochemical characteristics of some of the SDs.

# 6 Conclusions

(1) Three kinds of matrix dolomites are identified in the Dengying Formation in the southern Sichuan Basin: micritic dolomite, algal micritic dolomite, and FCD. Precipitation occurred in a seawater environment, but differences in the facies controlled the dolomitization mechanisms and intensities, which differ significantly according to geochemical data. Specifically, there are dramatic variations in the dolomitization characteristics of algal micritic dolomite with different bonding structures. Seven classes of Dengying Formation dolomites are developed in the fractures and vugs; these have prominently different petrologic and geochemical characteristics and can be correlated throughout the entire region in accordance with their diagenetic characteristics and sequences. Differences in the geochemical characteristics of fillings and matrix dolomites increase between the early and late stages. It is also found that the inclusion homogenization temperatures of most minerals have near-linear features that are relative to the diagenetic time limit. Saddle dolomite, bladed quartz, and siliceous dolomite are not controlled by geotemperature gradient changes, reflecting that exotic fluids brought by the tectonic movement of the late stage had a certain impact on the diagenetic evolution.

(2) The Dengying Formation in the southern Sichuan Basin experienced six phases of dolomite fluid activities overall, where dominant fluids that evolved from seawater, meteoric fresh water, formation water, and hydrothermal fluids occurred successively and respectively within the depositional stage, shallow burial stage, supergene stage, and moderate-late burial stage, in association with multiple stages of hydrocarbon generation and expulsion, large-scale orogenic movements, and the formation of various kinds of materials.

(3) Significant variations are evident in the dolomitization mechanisms and controlling factors in each phase of dolomite fluid activities. Specifically, during the depositional stage, the matrix dolomite geochemical differentiation and early-stage fillings in fractures and vugs were closely related to sedimentary facies belt distribution. At the shallow burial stage, dolomitization was driven by compaction, and diagenetic fluids transited from seawater to formation water when dolomite was still primarily distributed in the synsedimentary fractures and vugs. In the moderate-to-deep burial stage, the dolomitization mode was mainly expressed as a tectonic-driven and hydrothermal mode. In the late stage, geological fluids consisted of formation water formed in a restricted environment and hydrothermal fluids from the deep mantle, which were controlled by late Caledonian fluid in a low-migration potential region and early-Hercynian principal stress area, respectively.

## Acknowledgments

edited by Hao Qingqing

## References

Alonso-Zarza, A.M., Bustamante, L., Huerta, P., Rodríguez-Berriguete, Á., and Huertas, M.J., 2016. Chabazite and dolomite formation in a dolocrete profile: an example of a complex alkaline paragenesis in Lanzarote, Canary Islands. *Sedimentary Geology*, 337(3): 1–11.

Beckert, J., Vandeginste, V., and John, C.M., 2015. Exploring the geological features and processes that control the shape and internal fabrics of late diagenetic dolomite bodies (Lower Khuff equivalent–Central Oman Mountains). *Marine and Petroleum Geology*, 68(6): 325–340.

Bozkaya, O., Bozkaya, G., Uysal, I.T., and Banks, D.A., 2016. Illite occurrences related to volcanic-hosted hydrothermal mineralization in the Biga Peninsula, NW Turkey: implications for the age and origin of fluids. *Ore Geology Reviews*, 76(4): 35–51.

Calugaru, I.L., Neculita, C.M., Genty, T., Bussière, B., and Potvin, R., 2016. Performance of thermally activated dolomite for the treatment of Ni and Zn in contaminated neutral drainage. *Journal of Hazardous Materials*, 310(11): 48–55.

Chen Daizhao, Zhou Xiqiang, Fu Yong, Wang Jiangguo and Yan Detian, 2015. New U-Pb zircon ages of the Ediacaran–Cambrian boundary strata in South China. *Terra Nova*, 27(1): 62–68.

Chen Zongqing, 2013. On five crustal movements and petroleum exploration in Lower Paleozoic Sichuan Basin. *China Petroleum Exploration*, 18(5): 15–23 (in Chinese with English abstract).

Davies, G.R., and Smith J.R., 2006. Structurally controlled hydrothermal dolomite reservoir facies: an overview. *AAPG Bulletin*, 90(11): 1641–1690.

Faure, G., 1977. *Principles of Isotope Geology*. New York: John Wiley Sons, 97–146.

Gerald, M., Friedman and John, E., Sanders, 1967. Chapter 6 origin and occurrence of dolostones. Developments in Sedimentology, 9(A): 267–348.

Gu Zhidong, Yin Jifeng, Jiang Hua, Zhang Baomnin, Li Qiufen, Yuan Miao, Zai Xiufen, Zhang Li and Yang Fan, 2016. Tectonic evolution from Late Sinian to Early Paleozoic and natural gas exploration in northwestern Sichuan Basin, SW China. *Petroleum Exploration and Development*, 43(1): 1–11 (in Chinese with English abstract).

Haeri-Ardakani, O., AL-Aasm, I., and Coniglio, M., 2013. Fracture mineralization and fluid flow evolution: an example from Ordovician–Devonian carbonates, southwestern Ontario. *Canada Geofluids*, 13(1): 1–20.

Huang Sijing, 2010. *Carbonate diagenesis*. Geological Publishing House (in Chinese with English abstract).

Huang Sijing, Huang Yu, Lan Yefang and Huang Keke, 2011. A comparative study on strontium isotope composition of dolomites and their coeval seawater in the Late Permian-Early Triassic, NE Sichuan basin. *Acta Petrologica Sinica*, 27(12): 3831–3842 (in Chinese with English abstract).

Huang Sijing, Tong Hongpeng, Liu Lihong, Hu Zuowei, Zhang Xuehua, Huan Jinlai and Huang Keke, 2009. Petrography, geochemistry and dolomitization mechanism of Feixianguan dolomites in Triassic, NE Sichuan, China. *Acta Petrologica Sinica*, 25(10): 2363–2372 (in Chinese with English abstract).

Huang Zhicheng, Chen Zhina, Yang Shouye and Liu Yan, 1999.

Primary $\delta^{13}$C and $\delta^{18}$O value in marine carbonates and the sea water temperature of Dengyingxia age in South China. *Journal of Palaeogeography*, 1(3): 1–7 (in Chinese with English abstract).

Husmann, M., Zuber, C., Maitz, V., Kienberger, T., and Hochenauer, C., 2016. Comparison of dolomite and lime as sorbents for in-situ H₂S removal with respect to gasification parameters in biomass gasification. *Fuel*, 181(10): 131–138.

Jacquemyn, C., Desouky, H.E., Hunt, D., Casini, G., and Swennen, R., 2014. Dolomitization of the Latemar platform: fluid flow and dolomite evolution. *Marine and Petroleum Geology*, 55(8): 43–67.

Jiang Yuqiang, Tao Yanzhong, Gu Yifan, Wang Yubo, Qiang Zitong, Jiang Na, Lin Gang and Jiang Chan, 2016. Hydrothermal dolomitization in Sinian Dengying Formation, Gaoshiti-Moxi area, Sichuan Basin, SW China. *Petroleum Exploration and Development*, 43(1): 51–60 (in Chinese with English abstract).

Jones, B. and Luth, R.W., 2002. Dolostones from Grand Cayman, British West Indies. *Journal of Sedimentary Research*, 72(4): 559–569.

Korte, C., Jasper, T., Kozur, H.W., Veizer, J., 2006. $^{87}$Sr/$^{86}$Sr record of Permian seawater. *Palaeogeography, Palaeoclimatology, Palaeoecology*, 240(1): 89–107.

Land, L.S., 1967. Diagenesis of skeletal carbonates. *Journal of Sedimentary Research*, 37(3): 914–930.

Land, L.S., 1980. The isotopic and trace element geochemistry of dolomite: the state of the art. *The Society of Economic Paleontologists and Mineralogists*, 28: 87–110.

Le Changshuo, 1984. *Petrology*. Beijing: Geological Publishing House (in Chinese with English abstract).

Lei Huaiyan and Zhu Lianfang, 1992. Study of origin of the Sinian algal and nonalgal dolomites in Sichuan Basin. *Acta Sedimentologica Sinica*, 10(2): 69–78 (in Chinese with English abstract).

Li Guorong, Wu Hengzhi, Ye Bing, Liu Zhrngzhong, Peng Bo, Wu Yajun, Peng Guangming and Zhu Yongyuan, 2014. Stages and mechanism of dissolution in Changhsing reservoir, Yuanba area. *Acta Petrologica Sinica*, 30(3): 709–717(in Chinese with English abstract).

Li Qigui, Li Kesheng, Zhou Zhuozhu, Yan Jihong and Tang Huanyang, 2013. Palaeo geomorphology and karst distribution of Tongwan unconformity in Sichuan Basin. *Oil and Gas Geology*, 34(4): 516–521 (in Chinese with English abstract).

Li Qing, Jiang Zaixing, Hu Wenxuan, You Xuelisn, Hao Guoli, Zhang Juntao and Wang Xiaolin, 2016. Origin of dolomites in the Lower Cambrian Xiaoerbulak Formation in the Tarim Basin, NW China: implications for porosity development. *Journal of Asian Earth Sciences*, 115(1): 557–570.

Lian Chengbo, Qu Fang, Tan Xiucheng, Li Ling, Jin Mindong, Zen Wei, Ren Quanxiong, Hu Guang and Liu Hong, 2016. Occurrences and formation mechanisms of botryoidal structures from the Sinian Dengying Formation, Sichuan Basin, China. *Acta Geologica Sinica* (English Edition), 90(1): 384–385.

Lin Xiaoxian, Peng Jun, Du Lingchun, Yan Jianping and Hou Zhongjian, 2017. Characterization of the microbial dolomite of the Upper Sinian Dengying Formation in the Hanyuan area of Sichuan Province, China. *Acta Geologica Sinica* (English Edition), 34(4): 516–521.

Lippmann, F., 2012. Sedimentary carbonate minerals. *Springer Science and Business Media*, 1–150.

Liu An, Ou Wenjjia, Wei Kai, Li Fang and Li Xubing, 2017. Characteristics of Dengying Formation paleo-reservoir in Daping County, Zhangjiajie, and its natural gas exploration significance. *Acta Geologica Sinica*, 91(8):1848–1859 (in Chinese with English abstract).

Liu Shugeng, Sun Wei, Wang Guozhi, Han Keyou, Li Zhiwu, Deng Bing, Ran Bo, Yong Zhiquan, Xu Guosheng, and Yuan Haifeng, 2013. Analysis of cause of oil and gas accumulation in superimposed Sichuan Basin of China. *Journal of Chengdu University of Technology* (Science & Technology Edition), 40 (5): 481–497 (in Chinese with English abstract).

Liu Xiaoping, Jin Zhijun, Bai Guoping, Guan Ming, Liu Jie, Pan Qinghua, Li Ting and Xing Yujie, 2017. Formation and distribution characteristics of Proterozoic–Lower Paleozoic marine giant oil and gas fields worldwide. *Petroleum Science*, 14(02): 237–260.

Lu Huanzhang, 2016. *Fluid Inclusions*. Beijing: Science Press (in Chinese with English abstract).

Ma Wenxin, Liu Shugen, Chen Cuihua, Huang Wenming, Zhang Changjun and Song Guangyong, 2011. Geochemical characteristics of the siliceous rock in the Upper Sinian Denying Formation in the eastern Chongqing, China. *Bulletin of Mineralogy, Petrology and Geochemistry*, 30(2): 160–170 (in Chinese with English abstract).

Machel, H.G., and Lonnee, J., 2002. Hydrothermal dolomite-A product of poor definition and imagination. *Sedimentary Geology*, 152(3): 163–171.

Meng Yuanlin, Zhu Hengdong, Li Xinning, Wu Chenliang, Hu Anwen, Zhao Zitong, Zhang Lei and Xu Cheng, 2014. Thermodynamic analyses of dolomite dissolution and prediction of the secondary porosity zones: A case study of tight tuffaceous dolomites of the second member, Permian Lucaogou Formation reservoir, Santanghu Basin, NW China. *Petroleum Exploration and Development*, 41(06): 690–696.

Morrow, D.W., and Aulstead, K.L., 1995. The Manetoe Dolomite --a Cretaceous-Tertiary or a Paleozoic event? Fluid inclusion and isotopic evidence. *Bulletin of Canadian Petroleum Geology,* 43: 267–280.

Peng Bo, Li Guorong, Li Zongxing, Liu Chenglin, Zuo Yinhui, Zhang Wen, Yuan Li, Zhao Sha and Yao Cheng, 2018. Discussion of multiple formation mechanisms of saddle dolomites—comparison of geochemical data of Proterozoic–Paleozoic dolomites. *Energy Exploration & Exploitation*, 36 (1): 66–96.

Ronchi, P., Masetti, D., Tassan, S., and Camocino, D., 2012. Hydrothermal dolomitization in platform and basin carbonate successions during thrusting: a hydrocarbon reservoir analogue (Mesozoic of Venetian Southern Alps, Italy). *Marine and Petroleum Geology*, 29(1): 68–89.

Shi Zejin, Wang Yong, Tian, Yaming, and Wang Changcheng, 2013. Cementation and diagenetic fluid of algal dolomites in the Sinian Dengying Formation in southeastern Sichuan Basin. *Science China: Earth Science*, 56(2): 192–202 (in Chinese with English abstract).

Sibley, D.F., and Gregg, J.M., 1987. Classification of dolomite rock textures. *Journal of Sedimentary Research*, 57(6): 967–975.

Stein, M., Starinsky, A., Agnon, A., Katz, A., Raab, M., Spiro, B., and Zak, I., 2000. The impact of brine-rock interaction during marine evaporite formation on the isotopic Sr record in

the oceans: evidence from MtSedom, Israel. *Geochimica et Cosmochimica Acta*, 64(12): 2039–2053.

Su Jin, Wang Yu, Wang Xiaomei, He Kun, Yang Haijun, Wang Huitong, Wang Huajian, Zhang Bin, Huang Ling, Weng Na, Bi Lina and Xiao Zhihua, 2017. Impact of formation water on the generation of H2S in condensate reservoirs: a case study from the deep Ordovician in the Tazhong uplift of the Tarim Basin, NW China. *Petroleum Science*, 14(03): 507–519.

Urey, H.C., 1947. The thermodynamic properties of isotopic substances. *Journal of the Chemical Society* (Resumed): 562–581.

Urey, H.C., Epstein, S., McKinney, C., and McCrea, J., 1948. Method for measurement of paleotemperatures. *Geological Society of America Bulletin*, 59(12): 1359–1360.

Wang Guozhi and Liu Shugeng, 2009. Paleo-fluid geochemical evaluation of hydrocarbon preservation in marine carbonate rock areas: Taking lower association in central Sichuan Basin as an example. *Journal of Chengdu University of Technology* (Science & Technology Edition), 36(6): 631–644 (in Chinese with English abstract).

Wang Guozhi, Liu Shugeng, Chen Cuihua, Wang Dong and Sun Wei, 2013. The genetic relationship between MVT Pb-Zn deposits and paleo-oil/gas reservoirs at Heba, Southeastern Sichuan Basin. *Earth Science Frontiers*, 20(1): 107–116 (in Chinese with English abstract).

Wang Guozhi, Liu Shugeng, Li Na, Wang Dong and Gao Yuan, 2014. Formation and preservation mechanism of high quality reservoir in deep burial dolomite in the Dengying Formation on the northern margin of the Sichuan basin. *Acta Petrologica Sinica*, 30(3): 667–678.

Wang Lichao, Hu Wenxuan, Wang Xiaolin, Cao Jian and Chen Qi, 2014. Seawater normalized REE patterns of dolomites in Geshan and Panlongdong sections, China: Implications for tracing dolomitization and diagenetic fluids. *Marine and Petroleum Geology*, 56(9): 63–73.

Wang Xiaolin, Wan Ye, Hu Wenxuan, You Donghua, Cao Jian, Zhu Dongya and Li Zhen, 2017. Experimental studies on the interactions between dolomite and SiO2-rich fluids: implications for the formation of carbonate reservoirs. Geological Review, 63(6): 1639–1652 (in Chinese with English abstract).

Wood, W.W., Sanford, W.E., and Al Habshi, A.R.S., 2002. Source of solutes to the coastal sabkha of Abu Dhabi. *Geological Society of America Bulletin*, 114(3): 259–268.

Xi Binbin, Yu Xiaolu, Wang Jie, Jiang Hong and Zhang Jun. Character of fluid inclusions in quartz and dolomite cements of the Yuanba gas reservoir, NE Sichuan, China and its geological significance. *Acta Geologica Sinica*, 91(9): 2090–2104 (in Chinese with English abstract).

Xu Guosheng, Liang Jiaju, Gong Deyu, Wang Guozhi, Yuan Haifeng, Cao Junxing and Zhang Chengfu, 2013. Fluid migration paths in the marine strata of typical structures in the western Hubei-eastern Chongqing area. China. *Petroleum Science*, 10(1): 1–18.

Xu Guosheng, Yuan Haifeng, Ma Yongsheng, Liu Shugeng, Cai Xunyu, Wang Guozhi and Pan Changlin, 2007. The source of Sinian and Lower Palaeozoic bitumen and hydrocarbon

evolution in the middle and southeast of the Sichuan Basin. *Acta Geologic Sinica*, 81(8): 1143–1152.

You Xuelian, Lin Changsong, Zhu Jingquan and Tan Junying, 2015. Primary microbial dolomite precipitation in culture experiments and in stromatolite formations: implications for the dolomite problem. *Carpathian Journal of Earth and Environmental Sciences*, 10(3): 197–206.

You Xuelian, Sun Shu and Zhu Jingquan, 2014. Significance of fossilized microbes from the Cambrian stromatolites in the Tarim Basin, Northwest China. *Science China: Earth Sciences*, 57(12): 2901–2913.

You Xuelian, Sun Shu, Zhu Jingquan, Li Qing, Hu Wenxuan and Dong Hailiang, 2013. Microbially mediated dolomite in Cambrian stromatolites from the Tarim basin, northwest China: implications for the role of organic substrate on dolomite precipitation. *Terra Nova*, 25(5): 387–395.

Yuan Haifeng., Liu Yong, Xu Fanghao, Wang Guozhi and Xu Guosheng, 2014. The fluid charge and hydrocarbon accumulation, Sinian reservoir, Anpingdian-Gaoshiti Structure, Central Sichuan Basin. *Acta Petrologica Sinica*, 30 (3): 727–736.

Yuan Jianying, Huang Chenggang, Xia Qingsong, Cao Zhenglin, Zhao Fan, Wan Chuanzhi and Pan Xing, 2017. The characteristics of carbonate reservoir and formation mechanism of pores in the saline lacustrine basin: a case study of the Lower Eocene Ganchaigou Formation in western Qaidam Basin. *Geological Review*, 62(1): 111–126 (in Chinese with English abstract).

Zhang Juntao, Hu Wenxuan, Qian Yixiong, Wang Xiaolin, Cao Jian, Zhu Jingquan, Li Qing and Xie Xiaomin, 2009. Formation of saddle dolomites in Upper Cambrian carbonates, western Tarim Basin (northwest China): implications for fault-related fluid flow. *Marine and Petroleum Geology*, 26(9): 1428–1440.

Zheng Min, Jia Chengzao, Wang Wenguang, Li Peng, Li Jianzhong, Wu Xiaozhi and Zhang Yongfeng, 2015. The relationship between tectonic evolution and oil-cracking gas accumulation in late stage for marine superimposed basin. *Natural Gas Geoscience*, 26(2): 277–291 (in Chinese with English abstract).

Zhu Dongya, Meng Qingqiang, Jin Zhijun, Liu Quanyou and Hu Wenxuan, 2015. Formation mechanism of deep Cambrian dolomite reservoirs in the Tarim Basin, Northwestern. China. *Marine and Petroleum Geology*, 59(1): 232–244.

Zhu Shifa, Yue Hui, Zhu Xiaomin, Sun Shuyang, Wei Wei, Liu Xin and Jia Ye. 2017. Dolomitization of felsic volcaniclastic rocks in continental strata: a study from the Lower Cretaceous of the A'nan Sag in Er'lian Basin, China. *Sedimentary Geology*, 353(5): 13–27.

## About the first author

PENG Bo, male; born in 1986 in Sichuan province; research assistant of Institute of Geomechanics, Chinese Academy of Geological Sciences. His current interest is reservoir lithology. Address: No11, Minzuyuan Road, Haidian District, Beijing 100081, China. E-mail: bo.steven.peng@gmail.com.